Dendritic computations captured by an effective point neuron model

Songting Li[a,b,c], Nan Liu[d,e], Xiaohui Zhang[d,e,1], David W. McLaughlin[f,g,h,i,j,1], Douglas Zhou[a,b,c,1], and David Cai[a,b,c,f,g,h,k]

[a]School of Mathematical Sciences, Shanghai Jiao Tong University, Shanghai 200240, China; [b]Institute of Natural Sciences, Shanghai Jiao Tong University, Shanghai 200240, China; [c]Ministry of Education Key Laboratory of Scientific and Engineering Computing, Shanghai Jiao Tong University, Shanghai 200240, China; [d]State Key Laboratory of Cognitive Neuroscience and Learning, Beijing Normal University, Beijing 100875, China; [e]IDG/McGovern Institute for Brain Research, Beijing Normal University, Beijing 100875, China; [f]Courant Institute of Mathematical Sciences, New York University, New York, NY 10012; [g]Center for Neural Science, New York University, New York, NY 10012; [h]Institute of Mathematical Sciences, New York University Shanghai, Shanghai 200122, China; [i]New York University Tandon School of Engineering, New York University, Brooklyn, NY 11201; [j]Neuroscience Institute of New York University Langone Health, New York University, New York, NY 10016; and [k]NYU Abu Dhabi Research Institute, New York University Abu Dhabi, Abu Dhabi, United Arab Emirates

Contributed by David W. McLaughlin, May 31, 2019 (sent for review March 14, 2019; reviewed by Larry Abbott and Dario L. Ringach)

Complex dendrites in general present formidable challenges to understanding neuronal information processing. To circumvent the difficulty, a prevalent viewpoint simplifies the neuronal morphology as a point representing the soma, and the excitatory and inhibitory synaptic currents originated from the dendrites are treated as linearly summed at the soma. Despite its extensive applications, the validity of the synaptic current description remains unclear, and the existing point neuron framework fails to characterize the spatiotemporal aspects of dendritic integration supporting specific computations. Using electrophysiological experiments, realistic neuronal simulations, and theoretical analyses, we demonstrate that the traditional assumption of linear summation of synaptic currents is oversimplified and underestimates the inhibition effect. We then derive a form of synaptic integration current within the point neuron framework to capture dendritic effects. In the derived form, the interaction between each pair of synaptic inputs on the dendrites can be reliably parameterized by a single coefficient, suggesting the inherent low-dimensional structure of dendritic integration. We further generalize the form of synaptic integration current to capture the spatiotemporal interactions among multiple synaptic inputs and show that a point neuron model with the synaptic integration current incorporated possesses the computational ability of a spatial neuron with dendrites, including direction selectivity, coincidence detection, logical operation, and a bilinear dendritic integration rule discovered in experiment. Our work amends the modeling of synaptic inputs and improves the computational power of a modeling neuron within the point neuron framework.

dendritic computation | synaptic current | synaptic integration | single-neuron dynamics | point neuron model

A single neuron performs extensive computations through active dendrites with rich biophysical properties and morphological structures (1, 2). In general, it is difficult to understand information processing in a neuron when receiving broadly distributed synaptic activities on its dendrites. Despite the complexity of dendrites, the information is presumably encoded via action potentials generated at the soma of a neuron. Therefore, for a large set of issues regarding neuronal information coding, one usually simplifies a spatial neuron as a single point representing its soma with the membrane potential dynamics modeled as a resistance–capacitance circuit (3, 4),

$$C\frac{dV}{dt} = I_{ion} + I_{syn}, \qquad [1]$$

where C is the membrane capacitance and V is the membrane potential at the soma. Here, I_{ion} is the intrinsic ionic current, and I_{syn} is the synaptic current. By modeling different I_{ion}, one can obtain a class of point neuron models, such as the leaky integrate-and-fire neuron and the Hodgkin–Huxley neuron (5). For the synaptic current I_{syn}, in general, the integration of all individual synaptic inputs originated from dendrites is phenomenologically incorporated into a linear summation of 2 effective excitatory (E) and inhibitory (I) synaptic currents arriving at the soma, that is,

$$I_{syn} = g_E(\varepsilon_E - V) + g_I(\varepsilon_I - V), \qquad [2]$$

where g_E and g_I are the effective E and I synaptic conductances at the soma, respectively; and ε_E and ε_I are the E and I reversal potentials, respectively.

Point neuron models with synaptic current taking the form of Eq. **2** have been extensively applied to both experimental and theoretical studies, including synaptic current decomposition (6, 7), synaptic conductance estimation (8–10), dynamic clamp stimulation (11, 12), and neuronal network dynamics modeling (13–20), etc. Despite the simplicity of the point neuron model in analysis and simulation, various important questions remain to be addressed. For instance, do the E and I synaptic currents arriving at the soma of a spatial neuron with dendrites follow

Significance

Modeling single-neuron dynamics is the first step to quantitatively understand brain computation. Yet, the existing point neuron models fail to capture dendritic effects, which are crucial for neuronal information processing. We derive an effective point neuron model, which incorporates an additional synaptic integration current arising from the nonlinear interaction between synaptic currents across spatial dendrites. Our model captures the somatic voltage response of a neuron with complex dendrites and is capable of performing rich dendritic computations. Besides its computational efficiency in simulations, our model suggests reexamination of previous studies involving the decomposition of excitatory and inhibitory synaptic inputs based on the existing point neuron framework, e.g., the inhibition is often underestimated in experiment.

Author contributions: S.L., N.L., X.Z., D.W.M., D.Z., and D.C. designed research; S.L., N.L., X.Z., D.Z., and D.C. performed research; S.L., D.Z., and D.C. contributed new reagents/analytic tools; S.L., N.L., X.Z., D.W.M., D.Z., and D.C. analyzed data; and S.L., N.L., X.Z., D.W.M., D.Z., and D.C. wrote the paper.

Reviewers: L.A., Columbia University; and D.L.R., University of California, Los Angeles.

The authors declare no conflict of interest.

Data deposition: The source code for our model has been deposited on GitHub at https://github.com/songting858/DIF_model.

[1]To whom correspondence may be addressed. Email: xhzhang@bnu.edu.cn, david.mclaughlin@nyu.edu, or zdz@sjtu.edu.cn.

This article contains supporting information online at www.pnas.org/lookup/suppl/doi:10.1073/pnas.1904463116/-/DCSupplemental.

a linear summation as described in Eq. **2**? Can the point neuron model reflect dendritic integration effects and implement dendritic computations? If not, how do we establish a point neuron model to capture the essence of dendritic functions?

Results

Integration of E and I Synaptic Currents Revealed in Electrophysiological Experiments. We first investigate these questions in a CA1 pyramidal neuron of rat hippocampal slices. The whole-cell recording is made from the soma of the pyramidal neuron with sampling frequency 100 kHz, and fluorescent dye Alexa Fluor 488 is loaded into the neuron via the recording pipette to visualize the dendritic tree (Fig. 1*A*). Microiontophoretic applications of E transmitter glutamate and I transmitter γ-aminobutyric acid (GABA) at the apical dendrite induce rapid membrane depolarizations and hyperpolarizations, respectively, with kinetics similar to those of natural excitatory postsynaptic potentials (EPSPs) and inhibitory postsynaptic potentials (IPSPs) elicited by extracellular electrical stimulation in the CA1 region, respectively (Fig. 1*B*) (21). For convenience, these iontophoretic responses are referred to hereafter as EPSPs and IPSPs. To assess the validity of the synaptic current modeling (Eq. **2**), we first need to determine the intrinsic ionic current and the passive parameters in the point neuron description of this pyramidal neuron (Eq. **1**). Early experiments demonstrate that, within the subthreshold regime, the dynamics of the somatic membrane potential of a pyramidal neuron can be described as a leaky integrator (22, 23). Therefore, in the absence of action potentials, the ionic current I_{ion} can be well characterized as $I_{ion} = g_L(\varepsilon_L - V)$, where ε_L is the resting potential about -60 mV measured from the soma of the pyramidal neuron. The passive parameters are determined as $g_L \sim 11.67$ nS and $C \sim 129.67$ pF by giving a hyperpolarizing step current -50 pA at the soma of the pyramidal neuron. By convention, we rescale the leak conductance and the capacitance by dividing the estimated area of the neuron to obtain $g_L = 0.134\,\mathrm{mS}\cdot\mathrm{cm}^{-2}$ and $C = 1\,\mu\mathrm{F}\cdot\mathrm{cm}^{-2}$.

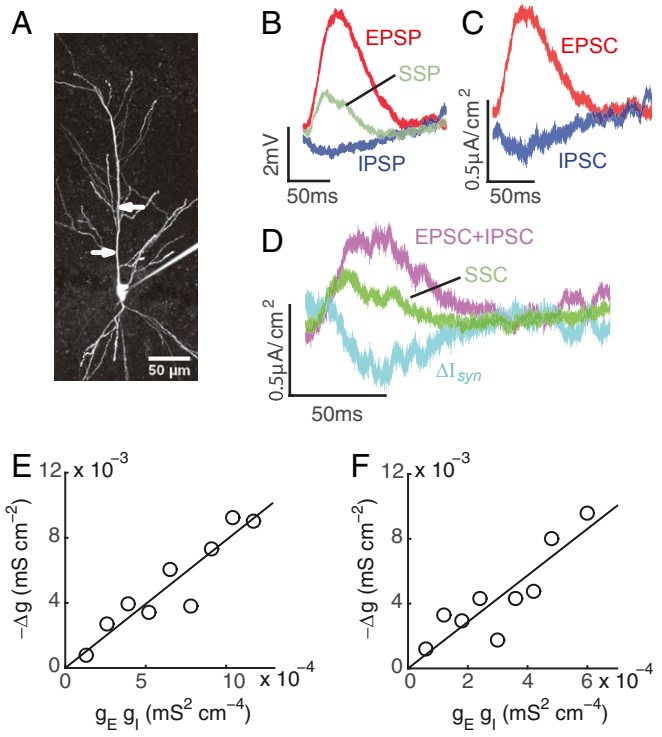

Fig. 1. Experimental measurement of the bilinear conductance relation for a pair of E and I inputs. (*A*) Image of a CA1 pyramidal neuron. Arrows indicate pipettes for iontophoresis of glutamate and GABA at about 100 and 50 μm from soma, respectively. (Scale bar: 50 μm.) (*B*) A set of individual EPSP, individual IPSP, and SSP induced by both E and I inputs recorded in the experiment. A simple moving average with time window of 5 ms is applied to smooth each trace. (*C*) Constructed EPSC and IPSC using the SSP and the E and I conductances estimated from the EPSP and IPSP in *B*. (*D*) The SSC estimated from the SSP in *B*, the linear sum of the constructed EPSC and IPSC in *C*, and the difference between them denoted as ΔI_{syn}. (*E*) The bilinear relation between Δg and the multiplication of g_E and g_I at the time when the EPSP reaches its peak value. The E and I inputs are given simultaneously. Line indicates linear fit (slope, $-\alpha_{EI} = 7.86\ \mathrm{k\Omega}\cdot\ \mathrm{cm}^2$, $R^2 = 0.87$). (*F*) The same as *E* except that the I input is given 20 ms preceded to the E input. Line indicates linear fit (slope, $-\alpha_{EI} = 14.35\ \mathrm{k\Omega}\cdot\ \mathrm{cm}^2$, $R^2 = 0.76$). In *E* and *F*, by varying the E and I input strengths, the amplitude of EPSP ranges from 1 to 8 mV, and the amplitude of IPSP ranges from -1 to -3 mV. For the purpose of denoising, we first measure values of g_E, g_I, and Δg for each set of EPSP, IPSP, and SSP; then, we construct a scatterplot of $g_E g_I$ vs. Δg, and finally, we divide the range of $g_E g_I$ into 9 bins and average all of the data points within each bin. In addition, similar results can be obtained by replacing moving average with low-pass filtering, such as the elliptic filter.

We next examine whether the E and I synaptic currents follow a linear summation as described in Eq. **2** when the pyramidal neuron receives synaptic inputs from its dendrites. In the experiment, when an E input is elicited by an iontophoretic pipette placed at the dendritic trunk ~ 100 μm away from the soma, an EPSP denoted as V_E is recorded at the soma. To eliminate the numerical error when taking the temporal derivative of the EPSP, we smooth the EPSP trace by performing simple moving average with time window 5 ms. Using the smoothed EPSP (Fig. 1*B*), the corresponding effective excitatory postsynaptic current (EPSC) denoted as I_E is derived based on the form of the point neuron model (Eq. **1**), that is, $I_E = C\frac{dV_E}{dt} - g_L(\varepsilon_L - V_E)$. Similarly, when an I input is elicited by an iontophoretic pipette placed at the dendritic trunk ~ 50 μm away from the soma, an IPSP denoted as V_I is recorded at the soma and smoothed by simple moving average (Fig. 1*B*), and the corresponding effective inhibitory postsynaptic current (IPSC) denoted as I_I is derived, that is, $I_I = C\frac{dV_I}{dt} - g_L(\varepsilon_L - V_I)$. Using the information of the EPSC and the IPSC, we further determine the effective E and I conductances at the soma as $g_E = I_E/(\varepsilon_E - V_E)$ and $g_I = I_I/(\varepsilon_I - V_I)$, respectively, with the E reversal potential $\varepsilon_E = 0$ mV and the I reversal potential $\varepsilon_I = -66$ mV measured from the experiment.

When both the E and I inputs are elicited simultaneously with the input strengths and locations the same as given individually, a summed somatic potential (SSP) denoted as V_S is recorded at the soma and smoothed by simple moving average (Fig. 1*B*), and the corresponding summed somatic current (SSC) denoted as I_S is derived as $I_S = C\frac{dV_S}{dt} - g_L(\varepsilon_L - V_S)$. Based on the synaptic current description (Eq. **2**) in the point neuron model, the SSC is presumably made of the linear summation of the E and I synaptic currents, that is, $I_S \equiv g_E(\varepsilon_E - V_S) + g_I(\varepsilon_I - V_S)$. However, by constructing the E and I synaptic currents, i.e., $g_E(\varepsilon_E - V_S)$ and $g_I(\varepsilon_I - V_S)$, using the resolved conductances g_E and g_I and the postsynaptic potential V_S (Fig. 1*C*), the SSC is found to be significantly different from instead of equal to the linear summation of the E and I synaptic currents (Fig. 1*D*). This fact demonstrates that the synaptic current description (Eq. **2**) is insufficient to characterize the synaptic current arriving at the soma as a result of dendritic integration.

To analyze the integration of synaptic currents quantitatively, we denote the difference between the SSC and the linear sum of the EPSC and the IPSC as the synaptic integration current ΔI_{syn}, that is, $\Delta I_{syn} = I_S - g_E(\varepsilon_E - V_S) - g_I(\varepsilon_I - V_S)$. If we cast this integration current in the form of Ohm's law as $\Delta I_{syn} = \Delta g(\varepsilon_E - V)$ with Δg defined as the integration conductance, by randomly varying the strengths of the E and I synaptic inputs with their input locations fixed, the integration conductance is found to

obey a bilinear rule throughout the response period until g_E or g_I vanishes (i.e., $\Delta g = \alpha_{EI} g_E g_I$, where α_{EI} is the proportional coefficient independent of the input strengths but dependent of time). Note that, when the synaptic integration current is cast in the form of Ohm's law, the reversal potential here is set to be the E reversal potential ε_E. We point out that the bilinear relation of the conductances remains valid when a different value of reversal potential is chosen (*SI Appendix*, Fig. S1), which will be further discussed in *Discussion*. The bilinear relation at a particular time point around the peak of the EPSP is illustrated in Fig. 1*E* (with coefficient of determination $R^2 = 0.87$). In addition, the bilinear relation remains valid even when there is a time delay between the E and I input arrival times. A particular case of the bilinear relation is shown in Fig. 1*F* ($R^2 = 0.76$) in which the I input is elicited 20 ms earlier than the E input. The proportional coefficients α_{EI} in both the concurrent and nonconcurrent inputs cases are not identical, indicating that α_{EI} is sensitive to input arrival time difference. Therefore, from our experiment, the synaptic current description (Eq. **2**) in the point neuron framework should be modified to incorporate the synaptic integration current ΔI_{syn}, and the corresponding integration conductance Δg follows a bilinear rule with the proportional coefficient α_{EI} independent of input strengths but dependent of time. For the ease of discussion, we refer to α_{EI} as the integration coefficient.

Integration of E and I Synaptic Currents Revealed in Realistic Neuron Simulations. To further confirm the existence and the structure of the synaptic integration current, we perform realistic neuron simulations in which the time derivatives of voltage can be precisely obtained to estimate the conductance values accurately. Here, a hippocampal CA1 pyramidal neuron model is built with a complex dendritic morphology (Fig. 2*A*) and active ionic channels (details of the model are in *Materials and Methods*). The E α-amino-3-hydroxy-5-methyl-4-isoxazolepropionic acid (AMPA) receptor and I $GABA_A$ receptor are implemented on the dendrites of the neuron with kinetics consistent with experimental recordings (21). The resting and reversal potentials are set as $\varepsilon_L = -70$, $\varepsilon_E = 0$, and $\varepsilon_I = -80$ mV. Similar to the experimental procedure, we first determine the passive parameters in the point neuron description of the pyramidal neuron model by injecting a step current at the soma of the neuron: $g_L = 0.11\ \mathrm{mS \cdot cm^{-2}}$ and $C = 1\ \mu\mathrm{F \cdot cm^{-2}}$. Then, in the simulation of the neuron model, an EPSP or an IPSP is measured at the soma (Fig. 2*B*) after eliciting an individual E synaptic input on the dendrite about 350 μm away from the soma or an individual I synaptic input about 280 μm away from the soma, respectively. The effective E and I conductances at the soma g_E and g_I are determined from the measured EPSP and IPSP, respectively. The neuron is then stimulated given both the E and I synaptic inputs simultaneously with the input strengths and input locations the same as given individually; an SSP is measured at the soma of the neuron, and the corresponding SSC is calculated. Consistent with our experimental observations, after constructing the EPSC and IPSC (Fig. 2*C*) using the E and I conductances and the SSP, the SSC is found to be significantly different from the linear summation of the constructed EPSC and IPSC (Fig. 2*D*). This indicates the existence of the synaptic integration current and challenges again the validity of the synaptic current form (Eq. **2**) in the point neuron framework.

Following the notation of the synaptic integration current ΔI_{syn} to denote the difference between the SSC and the linear summation of the constructed EPSC and IPSC, we next verify whether the integration conductance Δg obtained from ΔI_{syn} still follows a bilinear relation with the E and I conductances as observed in experiment. Assuming that ΔI_{syn} takes the form of Ohm's law [i.e., $\Delta I_{syn} = \Delta g(\varepsilon_E - V)$], by randomly varying the strengths of the E and I inputs with their input locations fixed, the integration conductance Δg is indeed shown to be proportional

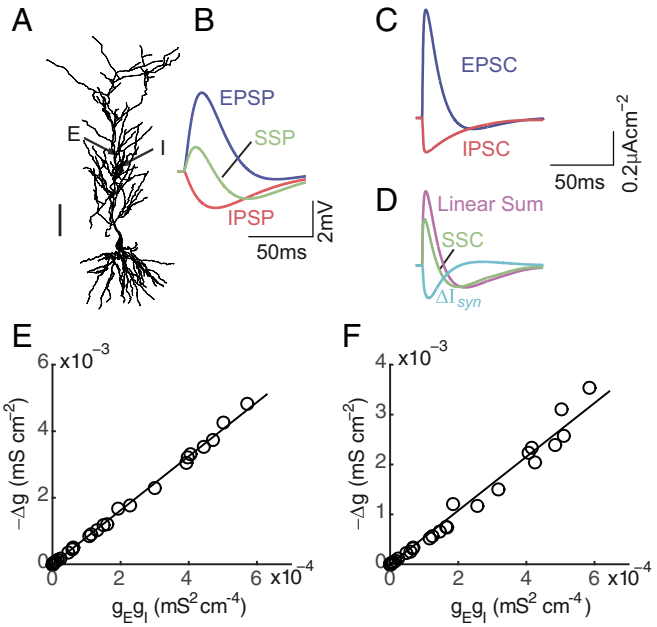

Fig. 2. Realistic neuron simulation result of the bilinear conductance relation for a pair of E and I inputs. (*A*) The reconstructed hippocampal CA1 pyramidal neuron. Arrows indicate that the I and E inputs are given on the dendritic truck about 280 and 350 μm away from the soma. (Scale bar: 100 μm.) Model details can be found in refs. 21, 24, and 25. (*B*) A set of simulated individual EPSP, individual IPSP, and SSP induced by both E and I inputs. (*C*) Constructed EPSC and IPSC using the SSP and the E and I conductances estimated from the EPSP and IPSP in *B*. (*D*) The SSC estimated from the SSP in *B*, the linear sum of the constructed EPSC and IPSC in *C*, and the difference between them denoted as ΔI_{syn}. (*E*) The bilinear relation between Δg and the multiplication of g_E and g_I at the time when the E conductance reaches its peak value. The E and I inputs are given simultaneously. Line indicates linear fit (slope, $-\alpha_{EI} = 8.12\ \mathrm{k\Omega \cdot\ cm^2}$, $R^2 = 0.998$). (*F*) The same as *E* except that the I input is given 20 ms preceded to the E input. Line indicates linear fit (slope, $-\alpha_{EI} = 5.39\ \mathrm{k\Omega \cdot\ cm^2}$, $R^2 = 0.979$). In *E* and *F*, by varying the E and I input strengths, the amplitude of EPSP ranges from 0 to 6 mV, and the amplitude of IPSP ranges from 0 to −3 mV. Each circle corresponds to a set of EPSP, IPSP, and SSP.

to both g_E and g_I at each time point, confirming the bilinear relation $\Delta g = \alpha_{EI} g_E g_I$. The bilinear relation at the peak time of the E conductance is illustrated in Fig. 2*E* ($R^2 = 0.998$). Furthermore, the bilinear relation remains valid when the E and I inputs arrive nonconcurrently. As an illustration, a particular case of the bilinear relation is shown in Fig. 2*F* ($R^2 = 0.979$) when the I input is elicited 20 ms earlier than the E input. Consistent with our experimental observations, the integration coefficient α_{EI} in the bilinear relation is found to be independent of input strengths but is dependent of input arrival times (*SI Appendix*, Fig. S2).

Mechanism Underlying the Synaptic Current Integration. To investigate the origin of the synaptic integration current ΔI_{syn}, we perform the static 2-port analysis and show that it emerges from the interaction of synaptic inputs across the spatial dendrites (*SI Appendix* has details). In particular, from our analysis, the integration coefficient α_{EI} in the bilinear conductance relation can be expressed as

$$\alpha_{EI} \approx K_{SS}\left(1 - \frac{K_{EI}}{K_{ES}}\right) + K_{SS}\frac{\varepsilon_I}{\varepsilon_E}\left(1 - \frac{K_{EI}}{K_{IS}}\right), \qquad [3]$$

where K_{EI}, K_{ES}, and K_{SS} are the transfer resistances between the locations of the E and I inputs, between the locations of the E input and the soma, and at the soma, respectively.

NEUROSCIENCE

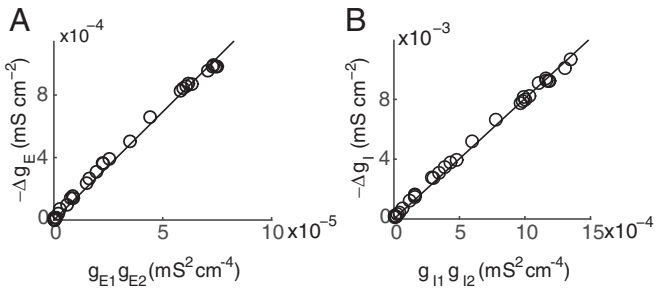

Fig. 3. Realistic neuron simulation result of the bilinear conductance relation for a pair of synaptic inputs of the identical type. (*A*) The bilinear relation between Δg_E and the multiplication of g_{E1} and g_{E2}. Data are collected by randomly changing the amplitude of EPSP from 0 to 4 mV. Line indicates linear fit (slope, $-\alpha_{EE} = 13.85\ \mathrm{k}\Omega \cdot\ \mathrm{cm}^2$, $R^2 = 0.994$). (*B*) The bilinear relation between Δg_I and the multiplication of g_{I1} and g_{I2}. Data are collected by randomly changing the amplitude of IPSP from 0 to −3 mV. Line indicates linear fit (slope, $-\alpha_{II} = 8.06\ \mathrm{k}\Omega \cdot\ \mathrm{cm}^2$, $R^2 = 0.999$). In *A* and *B*, the 2 E (I) inputs are given simultaneously on the dendritic trunk about 280 and 350 μm away from the soma, and the data are measured at the time when one of the E (I) conductances reaches its peak value.

Therefore, only in the limiting case when the E and I inputs are given at the soma, we have $K_{EI} = K_{ES} = K_{IS}$. In this case, according to Eq. **3**, the integration coefficient α_{EI} vanishes as does the synaptic integration current ΔI_{syn}, hence the validity of the synaptic current description (Eq. **2**). However, a neuron in general receives E and I inputs on the dendrites where $K_{EI} \neq K_{ES}$ and $K_{EI} \neq K_{IS}$. In such a case, according to Eq. **3**, α_{EI} deviates from zero; thus, the synaptic current description (Eq. **2**) fails to characterize the synaptic current arriving at the soma of a spatial neuron with dendrites. Note that our 2-port analysis shows that the synaptic integration current is mostly negative (*SI Appendix* has details), indicating an additional I effect at the soma coming from the synaptic integration in addition to hyperpolarizing and shunting effects of I inputs. Consequently, the form of the synaptic current (Eq. **2**) in the traditional point neuron framework underestimates the inhibition effect.

Integration of Identical-Type Synaptic Currents Revealed in Realistic Neuron Simulations. Via realistic neuron simulations, we further discover that the synaptic integration current and the bilinear conductance relation exist for cases of both a pair of E inputs and a pair of I inputs. When 2 inputs of the same type are elicited simultaneously on the dendrites of the realistic neuron about 350 and 280 μm away from the soma, the SSC derived from the point neuron model is found to deviate from the linear sum of 2 individual synaptic currents when elicited individually. The difference between them is also denoted as ΔI_{syn} and casted by the form of Ohm's law: that is, $\Delta I_{syn} = \Delta g_k(\varepsilon_k - V)$, where ε_k $(k = E, I)$ is the E or I reversal potential depending on the input type. By randomly varying the strengths of the 2 inputs without changing the input locations, the bilinear conductance relation can be observed as $\Delta g_E = \alpha_{EE} g_{E1} g_{E2}$ and $\Delta g_I = \alpha_{II} g_{I1} g_{I2}$, where α_{EE} and α_{II} are the integration coefficients independent of input strengths and g_{k1} and g_{k2} $(k = E, I)$ are the conductances measured when the 2 inputs are given separately. The bilinear relation at the time when one of the conductances reaches its peak value is illustrated in Fig. 3*A* for the case of 2 E inputs ($R^2 = 0.994$) and in Fig. 3*B* for the case of 2 I inputs ($R^2 = 0.999$). Additional simulation results demonstrate that the integration coefficients vary at different time points (Fig. 4*A*) and are dependent of input arrival times. Note that, for the cases of both a pair of E inputs and a pair of I inputs, the expressions of the integration coefficients α_{EE} and α_{II} in the bilinear conductance relation can be similarly obtained as in Eq. **3** using our 2-port analysis (*SI Appendix* has details), indicating the existence of the synaptic integration current in these cases.

Spatiotemporal Dependence of the Integration Coefficients. We next investigate the spatial dependence of the integration coefficients α_{EI}, α_{EE}, and α_{II} in realistic neuron simulations. For a pair of E and I inputs, when the I input location is fixed, the dependence of the integration coefficient α_{EI} on the E input location shows a clear asymmetry for proximal vs. distal E input locations. To be specific, given an I input on the dendritic trunk, $-\alpha_{EI}$ decreases rapidly as the distance between the E and I sites increases when the E input site is located between the soma and the I input site but remains constant when the E input site is located farther away from the soma than the I input site (Fig. 4*B*). In contrast, for a pair of E inputs, when 1 E input location is fixed, the dependence of the integration coefficient α_{EE} on the other E input location shows a clear symmetry for proximal vs. distal E input locations. Also, $-\alpha_{EE}$ is largest when the 2 E input sites overlap with each other and decays when the distance between the 2 E inputs increases (Fig. 4*C*). The spatial dependence of α_{II} is similar to that of α_{EE} (Fig. 4*D*). Accounting for the fact that a neuron receives the majority of synaptic inputs from its dendritic branches, we also investigate the spatial dependence of the integration coefficients on the whole dendrites. We find that the above spatial dependence of the integration coefficient still holds when 1 input site is fixed on the dendritic trunk and the other input site is scattered on the dendritic arbor (*SI Appendix*, Fig. S3). In addition, when 1 input site is fixed on a dendritic branch, the integration coefficient is significantly non-zero only when the other input site is within the same branch (*SI Appendix*, Fig. S3), consistent with the theory that each dendritic branch is an independent functional computational unit (26, 27). It has been further noticed that the integration coefficient for a pair of inputs within a branch is in general larger than that for 2 inputs at the dendritic trunk (*SI Appendix*, Fig. S3). All of these spatial properties of the integration coefficients observed in the simulations can be successfully explained from our 2-port analysis (*SI Appendix* has details).

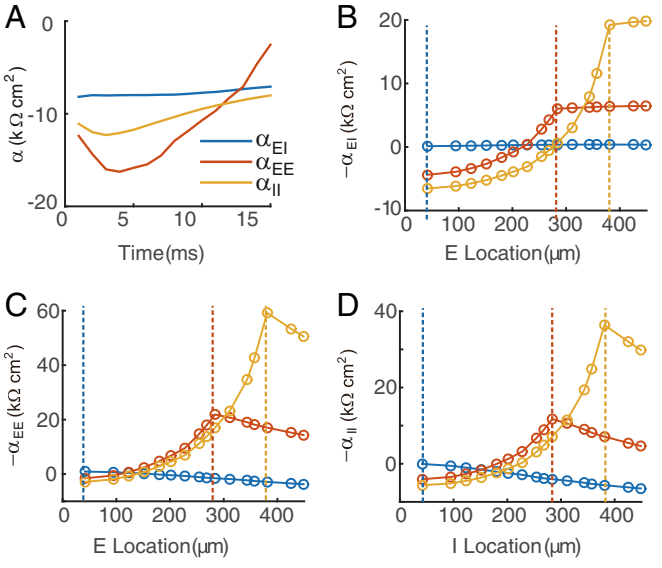

Fig. 4. Spatiotemporal properties of the integration coefficients. (*A*) α_{EE}, α_{II}, and α_{EI} as a function of time. (*B*) The spatial dependence of $-\alpha_{EI}$. For each color-coded curve, the I input is fixed at the location marked by the dashed line with identical color, and the E input moves along the dendritic trunk from the soma toward the distal dendrites. (*C* and *D*) The spatial profiles of $-\alpha_{EE}$ and $-\alpha_{II}$, respectively.

For the temporal dependence, although the integration coefficients are time dependent (Fig. 4*A*), the point neuron model can predict the SSP accurately by incorporating the synaptic integration currents with their coefficients approximated by time-independent constants as will be demonstrated in the simulation below. For a pair of E and I synaptic inputs, we first approximate the integration coefficient as a function of time by its value measured at the time when the E conductance reaches its peak value. The approximation can be justified by the fact that the integration conductance $\Delta g = \alpha_{EI} g_E g_I$ contributes dominantly to the synaptic integration current when $g_E g_I$ is around its peak, and Δg is insensitive to the value of α_{EI} when $g_E g_I$ approaches zero away from its peak. We then build the point neuron model by including the synaptic integration current with the approximated constant integration coefficient. Given a pair of E and I inputs separately, we can measure the E and I conductance transients and use them in the point neuron model with the synaptic integration current incorporated to predict the SSP when the pair of E and I inputs is given simultaneously. We then compare the predicted SSP with the simulated SSP obtained from the realistic neuron when it receives the 2 inputs simultaneously. The simulation result shows that, given a pair of E and I inputs at a dendritic branch about 230 and 200 μm away from the soma simultaneously, the predicted SSP from the point neuron model with the synaptic integration current incorporated almost overlaps with that recorded from the soma of the realistic neuron. In contrast, the SSP predicted by the point neuron model without the synaptic integration current deviates from the simulated SSP (Fig. 5*A*). Similar results are observed in the cases of a pair of E inputs and a pair of I inputs (Fig. 5 *B* and *C*). We note that the prediction error for the point neuron model without the synaptic integration current is significant (i.e., the relative error measured at the peak amplitude of the voltage trace is 248.9% for the E–I case, 20.8% for the E–E case, and 33.3% for the I–I case).

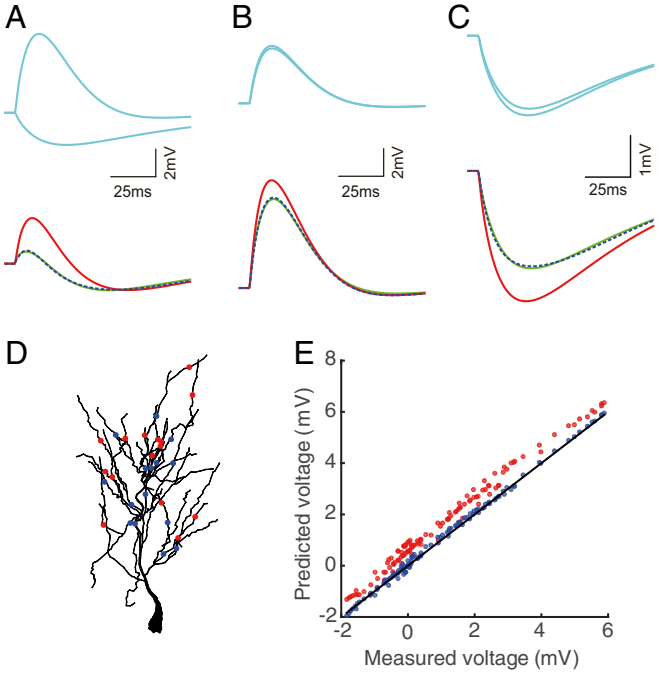

Fig. 5. Synaptic integration current captures the somatic voltage dynamics shaped by spatiotemporal dendritic integration. (*A*–*C*) The SSP produced by the realistic neuron model (green) given a pair of (*A*) E–I, (*B*) E–E, and (*C*) I–I inputs (cyan), the SSP predicted by the point neuron model with the synaptic integration current using a constant integration coefficient (dashed blue), and the SSP predicted by the point neuron model without the synaptic integration current (red). The 2 inputs are given at dendritic branches about 230 and 200 μm away from the soma. The integration coefficients in the 3 cases are $\alpha_{EI} = -18.05$, $\alpha_{EE} = -40.16$, and $\alpha_{II} = -27.21$ kΩ · cm^2, respectively. (*D*) Distribution of 15 E inputs (red dots) and 15 I inputs (blue dots) at the dendritic arbor in stratum radiatum of the realistic neuron model. (*E*) The SSPs predicted by the point neuron model with (blue) and without (red) the synaptic integration current are plotted against the measured SSP from the simulation of the realistic neuron model. The membrane potential from the realistic neuron model is obtained by setting the E and I inputs at locations shown in *D*, with the input arrival time at each location uniformly randomly distributed from 0 to 200 ms. For the ease of comparison, the slope of the black line is unity.

Generalization of Synaptic Integration Current for Multiple Synaptic Inputs. When a neuron receives multiple E and I inputs, the synaptic current can be naturally generalized as

$$I_{syn} = \sum_i g_E^i(\varepsilon_E - V) + \sum_j g_I^j(\varepsilon_I - V) + \Delta I_{syn}, \qquad [4]$$

where the synaptic integration current ΔI_{syn} is described as

$$\Delta I_{syn} = \sum_m \sum_n \alpha_{EI}^{mn} g_E^m g_I^n(\varepsilon_E - V) + \sum_p \sum_q \alpha_{EE}^{pq} g_E^p g_E^q(\varepsilon_E - V) + \sum_s \sum_t \alpha_{II}^{st} g_I^s g_I^t(\varepsilon_I - V). \qquad [5]$$

The synaptic integration current describes the interaction of each paired input, and the sets of integration coefficients $\{\alpha_{EI}^{mn}\}$, $\{\alpha_{EE}^{pq}\}$, and $\{\alpha_{II}^{st}\}$ encode the spatiotemporal information of synaptic inputs on the dendrites. In addition to the synaptic current description (Eq. **4**), by incorporating the synaptic integration current (Eq. **5**), the model accurately characterizes the synaptic currents arriving at the soma. As demonstrated from our numerical simulations, when the realistic neuron model receives 15 E synaptic inputs and 15 I synaptic inputs from its dendrites with uniformly distributed arrival times (Fig. 5*D*), its somatic voltage nearly overlaps with the SSP predicted by the point neuron model with the synaptic integration current while deviating from the SSP predicted by the point neuron model without the synaptic integration current (Fig. 5*E*).

Through electrophysiological experiments, realistic neuron simulations, and theoretical analyses, we demonstrate the existence of the synaptic integration current and the bilinear conductance relation with the integration coefficient encoding the spatiotemporal information of synaptic inputs on the dendrites of a spatial neuron. Under the point neuron framework, we show that the point neuron model by incorporating the synaptic integration current can accurately predict the somatic membrane potential of a spatial neuron with dendrites in response to synaptic inputs. Our results demonstrate that the spatiotemporal interaction among multiple synaptic inputs on the high-dimensional, nonlinear, active dendrites of a neuron can be decomposed into pairwise interactions for all pairs of synaptic inputs. In addition, the interaction between each pair of synaptic inputs can be reliably parameterized by a single integration coefficient, suggesting the inherent low-dimensional structure of the dendritic integration process.

Dendritic Phenomena Captured by the Synaptic Integration Current. We next give 2 examples to illustrate that the derived point neuron model with the synaptic integration current incorporated is capable of capturing dendritic effects.

Countering dendritic filtering effect. Our derived point neuron model predicts a phenomenon of dendritic filtering effect. Early experiments have shown that a local E synaptic input on the dendrite will be filtered by the dendritic cable property, resulting in a broader EPSP at the soma than that measured on the dendrite.

This is known as the dendritic filtering effect. Because of this effect, the rising time of the somatic EPSP becomes slower as the distance between the E input location and the soma increases, indicating that the neuron may respond slower to inputs received at distal dendrites than at proximal dendrites (28). However, the existence for the synaptic integration current predicts that the dendritic filtering effect can be alleviated or even reversed in the presence of an I input. Given both E and I inputs, the effective E conductance becomes $g_E(1+\alpha_{EI}\,g_I)$. Despite the fact that the E conductance g_E (derived from the EPSC at the soma when the E input is given alone) rises slower for the input received at the distal dendrites than at the proximal dendrites, the effective E conductance $g_E(1+\alpha_{EI}\,g_I)$ can be shown to rise even faster for the distal E input with a large negative α_{EI} (Fig. 6 *A*, *Left*). Therefore, the SSP induced by the distal E input could rise faster than that induced by the proximal E input, countering the dendritic filtering effect (Fig. 6 *A*, *Left*).

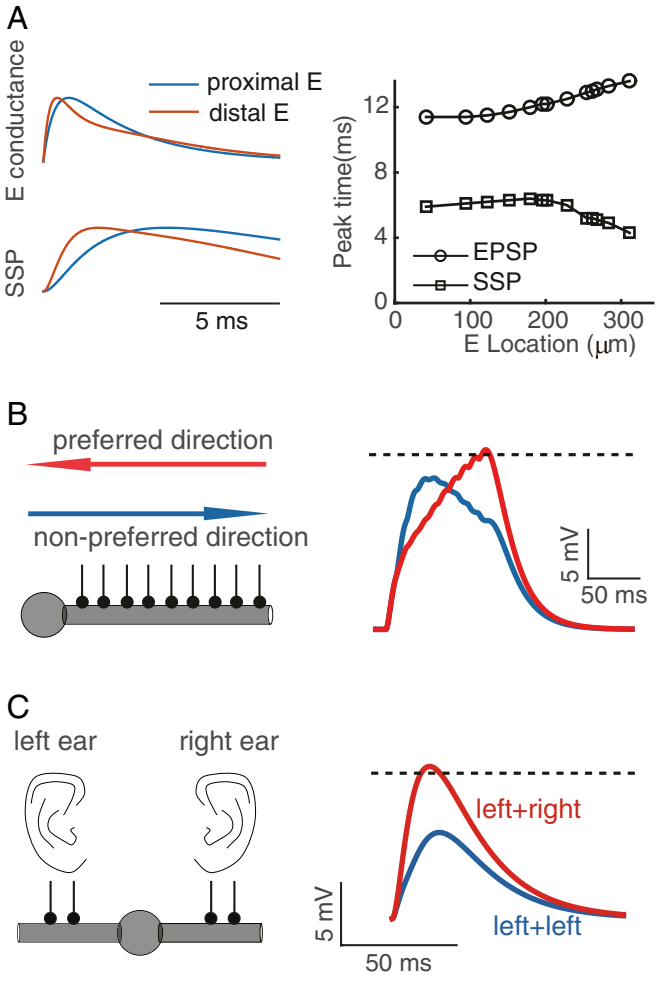

Fig. 6. Dendritic computations in a point neuron model with the synaptic integration current. (*A*) The countering dendritic filtering effect. In the presence of an I input, (*A*, *Upper Left*) the E conductance $g_E(1+\alpha_{EI}g_I)$ exhibits a faster rising time for a distal E input (red) than a proximal E input (blue). (*A*, *Lower Left*) The SSPs induced by both E and I inputs from the point neuron model with the synaptic integration current, which also exhibits a faster rising time for a distal E input (red) than a proximal E input (blue). (*A*, *Right*) The location dependence of the rising time of the individual EPSP and the SSP obtained in realistic neuron simulations. If an I input is elicited, its location is on the trunk about 250 μm away from the soma. All voltages are normalized to have an identical amplitude. (*B*, *Left*) Schematic plot of the dendritic mechanism for direction selectivity. The red arrow indicates the preferred direction along which the activation of synapses will promote the activity of the neuron, while the blue arrow indicates the nonpreferred direction that has the opposite effect. (*B*, *Right*) The realization of direction selectivity in a point neuron model with the synaptic integration current for the preferred direction (red) and the nonpreferred direction (blue). (*C*, *Left*) Schematic plot of the dendritic mechanism for coincidence detection. Detection of coincident inputs is facilitated when the inputs are received on 2 separate branches. (*C*, *Right*) The realization of coincidence detection in a point neuron model with the synaptic integration current for the 2 inputs received on different branches (red) and on the same branch (blue). In *B* and *C*, the dashed lines indicate the firing threshold.

The predicted effect of countering dendritic filtering has been verified in realistic neuron simulations in which an I input is fixed in the middle of the dendritic trunk and an E input moves from the soma toward the distal dendrites. Simulation results demonstrate that, when only an E input is given on the dendrites, the time when the somatic EPSP reaches its peak value increases as the distance between the E input and the soma increases; however, when both E and I inputs are given on the dendrites, the time when the SSP reaches its peak value decreases as the distance between the E input and the soma increases (Fig. 6 *A*, *Right*). In addition to the phenomenon of countering dendritic filtering per se, the successful prediction made from the synaptic integration current suggests that one can investigate complex dendritic computations through the analysis of the simple form of the derived synaptic integration current as discussed above.

Bilinear dendritic integration rule. Our point neuron model with the synaptic integration current incorporated is capable of capturing a bilinear rule of dendritic integration discovered in recent experiments (21, 24). In the experiments (21, 24), given a pair of glutamatergic E input and GABAergic I input simultaneously to a hippocampal CA1 pyramidal neuron, the SSP measured at the soma denoted by V_S can be well characterized by a bilinear rule as $V_S = V_E + V_I + k_{EI}\cdot V_E\,V_I$, where V_E and V_I are the EPSP and IPSP measured at the soma when the E or I input is given alone, respectively, and k_{EI} is the shunting coefficient, which depends on the dendritic locations and arrival times of the E and I inputs but not the strengths of the inputs. In particular, the spatial dependence of k_{EI} measured at the time when the EPSP reaches its peak value exhibits the feature of spatial asymmetry: when the location of the I input is fixed on the dendritic trunk and the E input is located between the soma and the I input site, k_{EI} increases as the distance between the E input and the soma increases; when the E input is located farther away from the soma than the I input site, k_{EI} remains constant with further increase in the distance between the E input site and the soma. The bilinear rule of dendritic integration has also been observed for the integration of a pair of E inputs, a pair of I inputs, and a mixture of multiple E and I inputs in both experiments and realistic neuron simulations (24).

We point out that the point neuron model including the synaptic integration current can reliably capture the bilinear dendritic integration rule and its generalizations, and the shunting coefficient k_{uv} can be determined by the integration coefficient α_{uv} $(u, v = E \text{or} I)$ (23). Furthermore, by using the 2-port analysis, we show that there is a linear mapping between the shunting coefficient k_{uv} and the integration coefficient α_{uv} (*SI Appendix* has details). From this mapping, one can elucidate the underlying mechanism of the bilinear dendritic integration rule and the spatially asymmetric feature of the shunting coefficient observed in the above experiment.

Dendritic Computations Performed by the Synaptic Integration Current. Here, we show that the point neuron model with the synaptic integration current incorporated possesses the computational power of a spatial neuron with dendrites.

Direction selectivity. A point neuron with the synaptic integration current is capable of performing the computation of

direction selectivity. As predicted by Rall's cable theory (29), the activation of a train of E inputs can promote the firing of a neuron when the inputs are received sequentially from the distal dendrite toward the soma but demote the firing when the E inputs are received in the reverse direction (Fig. 6*B*). In this way, the neuron has a preferred direction of input sequence. The sensitivity to spatiotemporal sequences of synaptic activation in cortical pyramidal neuron dendrites was observed in later experiments (2). In our derived synaptic integration current, the information of the input direction can be encoded in an ordered sequence of integration coefficients. In particular, the early activation of a pair of distal E inputs corresponds to the synaptic integration current with a large negative α_{EE}, and the late activation of a pair of proximal E inputs corresponds to the synaptic integration current with a small negative α_{EE} (*SI Appendix* has details). Therefore, given a temporal sequence of identical E inputs to the point neuron, its firing will be promoted by sequentially activating the set of α_{EE} with values that are in an increasing order but demoted by activating the set of α_{EE} in the reversed order (Fig. 6*B*).

Coincidence detection. Similarly, a point neuron with the synaptic integration current can play the role of coincidence detector. In the early auditory pathway, neurons that receive bilateral inputs have bipolar dendrites, with each dendritic tree receiving input from only 1 ear (30). These neurons can detect input coincidence with submillisecond temporal resolution in their role of computing interaural arrival time difference, which is a cue for sound localization (Fig. 6*C*). In the point neuron model with the synaptic integration current, the detection of coincident inputs can be facilitated by a small negative α_{EE} in the synaptic integration current for a pair of E inputs representing the case of the inputs received on separate dendrites and will be depressed by a large negative α_{EE} in the corresponding synaptic integration current representing the case of the inputs received on the same dendrite (Fig. 6*C* and *SI Appendix* have details).

Logical operation. The synaptic integration current enables a point neuron to perform logical operation. Previous studies have shown that one of the important functions of dendrites is to perform logical computation (3, 26). For instance, given a pair of E and I inputs, the I input is found to be maximally effective to silence the E input when the I input is received between the soma and the location of the E input, known as the "on-the-path effect" (3, 26). Therefore, given a pair of distal E synapse and proximal I synapse, to observe an output at the soma, it is required that the E synapse is activated, while the I synapse remains inactivated. Therefore, this pair of E and I inputs performs the logical operation of "E AND (NOT I)." In contrast, for an I input located farther away from the soma than the location of the E input—the out-of-the-path configuration—studies have shown that the I input exerts a weak influence on the E input. Therefore, this pair of E and I inputs no longer performs the logical operation of E AND (NOT I) but simply the gate of E. In addition, a pair of E inputs received at 2 separated branches in general will produce larger response at the soma of a neuron than a pair of E inputs received at the same branch. If the neuron requires at least 2 inputs to generate an output, the inputs are preferred to be at different branches. Therefore, 2 separate E inputs can play the role of an AND gate, while 2 nearby E inputs cannot. When a neuron receives multiple inputs distributed on the dendrites, the combination of the above-mentioned simple logical gates can give rise to complex logical operations. All of these logical operations can be easily achieved in the point neuron framework by measuring values of the integration coefficients in the synaptic integration current (Eq. **5**), because the integration coefficients encode the locations of inputs that determine the type of logical computations.

Discussion

In this work, by using electrophysiological experiments, realistic neuronal simulations, and theoretical analyses, we have derived a form of synaptic current in the point neuron framework as a result of dendritic integration. In addition to the traditional form of the synaptic current (Eq. **4**), our derived synaptic integration current described by Eq. **5** indicates that the interaction between each pair of synaptic inputs on the complex nonlinear active dendrites can be reliably captured by the bilinear interaction between their corresponding synaptic conductances. In addition, we have shown that the point neuron model with the synaptic integration current incorporated is able to capture many dendritic phenomena, including countering dendritic filtering, and a bilinear rule of dendritic integration discovered in a recent experiment, and the model possesses the computational ability of a spatial neuron with dendrites, including direction selectivity, coincidence detection, and logical operation.

When describing the synaptic integration current measured in our experiments and the simulations, we have chosen the reversal potential to be the E reversal potential. In fact, there is a degree of freedom for choosing the value of the reversal potential within the regime in which the ratio of the postsynaptic potential to the reversal potential is small, and the value of the integration coefficient α_{EI} depends on the choice of the reversal potential (*SI Appendix* has details). However, we stress that the bilinear interaction between the conductances remains valid when choosing a different reversal potential value (e.g., the I reversal potential), which has been justified in both our theoretical analysis (*SI Appendix*) and numerical simulations (*SI Appendix*, Fig. S1).

To reveal the mechanism underlying the existence of the synaptic integration current, for the simplicity of illustration, we have performed the steady-state analysis. By noticing that the static analysis fails to describe the temporal integration of synaptic inputs, we have also developed a strict analysis based on the dynamical cable equation when the model neuron receives time-dependent synaptic inputs. The dynamical analysis also gives rise to the identical form of synaptic integration current with time-dependent integration coefficients as a result of spatiotemporal dendritic integration.

According to the nonlinear integration between E and I conductances in the synaptic integration current, it behooves one to reexamine the ramifications of previous works involving the decomposition of E and I synaptic inputs. In many previous works, based on the form of the traditional synaptic current (Eq. **2**), by holding the somatic membrane potential at various levels using the voltage clamp, the E and I synaptic conductances (9) and currents (10) are estimated from the linear I–V relation where the slope is the total conductance $g_E + g_I$ and the intercept is the reversal current $g_E\varepsilon_E + g_I\varepsilon_I$. The measured conductances are often used to evaluate the state of a network (31). However, our work shows that the E and I conductances are not linearly separable but interact with each other nonlinearly. Therefore, the interpretation of the measured E and I components based on the traditional point neuron model is questionable.

We illustrate the issue of conductance measurement using realistic neuron simulations as shown in *SI Appendix*, Fig. S4. When a pair of E and I inputs is given at the dendritic trunk 350 and 280 μm away from the soma of the realistic neuron model separately, we calculate the E and I conductances in the corresponding point neuron model as the reference conductances. Note that the reference conductance is different from the local conductance at the dendrite; instead, it reflects directly the functional impact of local synaptic inputs on the somatic membrane potential change and thereby, neuronal information processing at the soma. When the same pair of E and I inputs is given at

the dendritic trunk simultaneously, by using the voltage clamp, the measured E and I conductances based on Eq. **2** significantly deviate from the reference conductances. In addition, in the case shown in *SI Appendix*, Fig. S4, the fact that inhibition is dominant to excitation can be misinterpreted as that E and I are approximately balanced. Through our analysis, the error is induced by neglecting the nonlinear integration between currents across the spatial dendrites when using the traditional point neuron framework.

It has been broadly believed that many dendritic phenomena, such as the integration of spatially distributed synaptic inputs, are beyond the scope of the existing point neuron models (32, 33). However, the dendritic integration process is known to have a strong impact on the action potential generation and thereby, neuronal information coding. Here, we have developed an effective point neuron model (i.e., a point neuron model with the synaptic integration current incorporated) that can capture many dendritic effects, and it has succinct structure for analysis and simulation. We have shown that the effective point neuron model can achieve the same order of accuracy for the somatic voltage dynamics as a detailed multicompartment model with substantially low computational costs (Fig. 5*D*).

Therefore, it is promising to develop fast algorithms for neuronal simulations to capture the dynamics of a neuron with realistic dendritic morphology. To be specific, the spatiotemporal profile of the integration coefficients encoding the information of synaptic inputs can be measured in advance and recorded in a library for future simulations. When simulating the point neuron model, the dendritic integration effect can be accurately captured by simulating the synaptic integration current with the integration coefficient read out from the library. It has been found in our simulation that the library of the integration coefficients is very sparse (*SI Appendix*, Fig. S5) (i.e., the majority of the coefficients are not large enough to induce a 5% change of SSP). This is consistent with previous works showing that the nonlinear interaction between a pair of inputs is mainly localized within a branch (26, 27). The sparsity of bilinear synaptic interactions benefits the simulation efficiency of our point neuron model. Consequently, the simulation speed is expected to be improved tremendously in comparison with simulating the realistic neuron model with full dendrites. The developed point neuron model in this work only describes the subthreshold regime without accounting for active channels associated with spike generation. However, this limitation could be potentially overcome by modeling the spike time as when the voltage reaches a firing threshold (i.e., the integrate-and-fire–type neuron). Another limitation of the developed point neuron model is that the integration current derived in our model so far only takes into account the second-order interaction of synaptic inputs; therefore, it may not be capable of capturing highly nonlinear dendritic phenomena, such as dendritic spikes and plateau potentials. Capturing these phenomena may involve the voltage dependence of the integration coefficients and higher-order interactions of synaptic inputs.

Furthermore, the form of the synaptic integration current reshapes the synaptic input modeling in both experiments and simulations. For instance, dynamic clamp has been extensively used in electrophysiological experiments, in which realistic E and I synaptic currents are generated at the soma of a neuron (34, 35) to mimic synaptic current dynamics. Based on our results, these synaptic currents are far from reality because of the neglect of the synaptic integration current. An appropriate way suggested by our results is to generate synaptic currents by incorporating the synaptic integration current (Eq. **5**) in future studies.

Materials and Methods

Slice Electrophysiology. The experimental procedure of whole-cell recording and microiontophresis on hippocampal CA1 pyramidal neurons in acute brain slices (350-μm thick) of juvenile Sprague–Dawley rats (postnatal days 15 to 20) followed the methods described in our previous study (21). The animal experimental protocols were approved by the Animal Use and Care Committee of the State Key Laboratory of Cognitive Neuroscience & Learning at Beijing Normal University (IACUC-BNU-NKLCNL-2016-02).

Realistic Neuron Simulation. We adapted the multicompartment neuron model used in our previous studies (21, 24, 25) for our realistic pyramidal neuron simulation. The morphology of the reconstructed pyramidal neuron, which includes 200 compartments, was obtained from the Duke–Southampton Archive of Neuronal Morphology (36). The passive cable properties and the densities of active conductances in the neuron model were based on published experimental data obtained from the hippocampal and cortical pyramidal neurons (27, 37–48). In particular, the multicompartment neuron model included the voltage-gated sodium channel, the delayed rectifier potassium channel, 2 variants of the A-type potassium channel, and the hyperpolarization activated channel. The E and I synaptic inputs were given through AMPA and $GABA_A$ receptors, respectively. The resting potential was set to $V_r = -70$ mV, and the E and I reversal potentials were set to $E_{AMPA} = 0$ and $E_{GABA_A} = -80$ mV. We used the NEURON software Version 7.4 (49) to simulate the model with a time step of 0.1 ms.

ACKNOWLEDGMENTS. We thank Li Yao for providing the neuron image in Fig. 1*A*. This work was supported by NYU Abu Dhabi Research Institute Grant G1301 (to S.L., D.Z., and D.C.); Shanghai Sailing Program 19YF1421400 (S.L.); Beijing Municipal Science & Technology Commission Grant Z181100001518001 (to X.Z.); Shanghai Grants 14JC1403800 and 15JC1400104 (to D.Z. and D.C.); Shanghai Rising-Star Program 15QA1402600 (to D.Z.); and Natural Science Foundation of China Grants 11671259, 11722107, 91630208 (all to D.Z.), and 3157107 (to D.C.).

1. M. London, M. Häusser, Dendritic computation. *Annu. Rev. Neurosci.* **28**, 503–532 (2005).
2. T. Branco, B. A. Clark, M. Häusser, Dendritic discrimination of temporal input sequences in cortical neurons. *Science* **329**, 1671–1675 (2010).
3. C. Koch, *Biophysics of Computation: Information Processing in Single Neurons* (Oxford University Press, 2004).
4. P. Dayan, L. F. Abbott, *Theoretical Neuroscience* (MIT Press, Cambridge, MA, 2001), vol. 31.
5. W. Gerstner, W. M. Kistler, *Spiking Neuron Models: Single Neurons, Populations, Plasticity* (Cambridge University Press, 2002).
6. N. J. Priebe *et al.*, Direction selectivity of excitation and inhibition in simple cells of the cat primary visual cortex. *Neuron* **45**, 133–145 (2005).
7. M. Wehr, A. M. Zador, Balanced inhibition underlies tuning and sharpens spike timing in auditory cortex. *Nature* **426**, 442–446 (2003).
8. S. J. Cruikshank, T. J. Lewis, B. W. Connors, Synaptic basis for intense thalamocortical activation of feedforward inhibitory cells in neocortex. *Nat. Neurosci.* **10**, 462–468 (2007).
9. J. S. Anderson, M. Carandini, D. Ferster, Orientation tuning of input conductance, excitation, and inhibition in cat primary visual cortex. *J. Neurophysiol.* **84**, 909–926 (2000).
10. C. Monier, J. Fournier, Y. Frégnac, In vitro and in vivo measures of evoked excitatory and inhibitory conductance dynamics in sensory cortices. *J. Neurosci. Methods* **169**, 323–365 (2008).
11. F. S. Chance *et al.*, Gain modulation from background synaptic input. *Neuron* **35**, 773–782 (2002).
12. Z. Piwkowska *et al.*, Characterizing synaptic conductance fluctuations in cortical neurons and their influence on spike generation. *J. Neurosci. Methods* **169**, 302–322 (2008).
13. D. McLaughlin, R. Shapley, M. Shelley, D. J. Wielaard, A neuronal network model of macaque primary visual cortex (v1): Orientation selectivity and dynamics in the input layer 4cα. *Proc. Natl. Acad. Sci. U.S.A.* **97**, 8087–8092 (2000).
14. L. Tao, M. Shelley, D. McLaughlin, R. Shapley, An egalitarian network model for the emergence of simple and complex cells in visual cortex. *Proc. Natl. Acad. Sci. U.S.A.* **101**, 366–371 (2004).
15. A. Compte, N. Brunel, P. S. Goldman-Rakic, X.-J. Wang, Synaptic mechanisms and network dynamics underlying spatial working memory in a cortical network model. *Cereb. Cortex* **10**, 910–923 (2000).
16. M. Rudolph, M. Pospischil, I. Timofeev, A. Destexhe, Inhibition determines membrane potential dynamics and controls action potential generation in awake and sleeping cat cortex. *J. Neurosci.* **27**, 5280–5290 (2007).
17. X. Zhang, K. M. Kendrick, H. Zhou, Y. Zhan, J. Feng, A computational study on altered theta-gamma coupling during learning and phase coding. *PLoS One* **7**, e36472 (2012).
18. D. Cai, A. V. Rangan, D. W. McLaughlin, Architectural and synaptic mechanisms underlying coherent spontaneous activity in v1. *Proc. Natl. Acad. Sci. U.S.A.* **102**, 5868–5873 (2005).

19. D. Zhou, A. V. Rangan, D. W. McLaughlin, D. Cai, Spatiotemporal dynamics of neuronal population response in the primary visual cortex. *Proc. Natl. Acad. Sci. U.S.A.* **110**, 9517–9522 (2013).
20. W. P. Dai, D. Zhou, D. W. McLaughlin, D. Cai, Mechanisms underlying contrast-dependent orientation selectivity in mouse v1. *Proc. Natl. Acad. Sci. U.S.A.* **115**, 11619–11624 (2018).
21. J. Hao, X.-d. Wang, Y. Dan, M.-m. Poo, X.-h. Zhang, An arithmetic rule for spatial summation of excitatory and inhibitory inputs in pyramidal neurons. *Proc. Natl. Acad. Sci. U.S.A.* **106**, 21906–21911 (2009).
22. L. Badel *et al.*, Extracting non-linear integrate-and-fire models from experimental data using dynamic i–v curves. *Biol. Cybernetics* **99**, 361–370 (2008).
23. D. Zhou, S. Li, X.-h. Zhang, D. Cai, Phenomenological incorporation of nonlinear dendritic integration using integrate-and-fire neuronal frameworks. *PLoS One* **8**, e53508 (2013).
24. S. Li, N. Liu, X.-h. Zhang, D. Zhou, D. Cai, Bilinearity in spatiotemporal integration of synaptic inputs. *PLoS Comput. Biol.* **10**, e1004014 (2014).
25. S. Li, D. Zhou, D. Cai, Analysis of the dendritic integration of excitatory and inhibitory inputs using cable models. *Commun. Math. Sci.* **13**, 565–575 (2015).
26. C. Koch, T. Poggio, V. Torre, Nonlinear interactions in a dendritic tree: Localization, timing, and role in information processing. *Proc. Natl. Acad. Sci. U.S.A.* **80**, 2799–2802 (1983).
27. P. Poirazi, T. Brannon, B. W. Mel, Pyramidal neuron as two-layer neural network. *Neuron* **37**, 989–999 (2003).
28. G. Stuart, N. Spruston, M. Häusser, *Dendrites* (Oxford University Press, 2016).
29. W. Rall, *The Theoretical Foundation of Dendritic Function: Selected Papers of Wilfrid Rall with Commentaries* (MIT Press, 1995).
30. H. Agmon-Snir, C. E. Carr, J. Rinzel, The role of dendrites in auditory coincidence detection. *Nature* **393**, 268–272 (1998).
31. Y. Shu, A. Hasenstaub, D. A. McCormick, Turning on and off recurrent balanced cortical activity. *Nature* **423**, 288–293 (2003).
32. W. Gerstner, R. Naud, How good are neuron models? *Science* **326**, 379–380 (2009).
33. A. V. M. Herz, T. Gollisch, C. K. Machens, D. Jaeger, Modeling single-neuron dynamics and computations: A balance of detail and abstraction. *Science* **314**, 80–85 (2006).
34. A. Destexhe, T. Bal, *Dynamic-Clamp: From Principles to Applications* (Springer, 2009).
35. A. A. Prinz *et al.*, The dynamic clamp comes of age. *Trends Neurosci.* **27**, 218–224 (2004).
36. R. C. Cannon, D. A. Turner, G. K. Pyapali, H. V. Wheal, An on-line archive of reconstructed hippocampal neurons. *J. Neurosci. Methods* **84**, 49–54 (1998).
37. A. Destexhe, Z. F. Mainen, T. J. Sejnowski, An efficient method for computing synaptic conductances based on a kinetic model of receptor binding. *Neural Comput.* **6**, 14–18 (1994).
38. A. Destexhe, Z. F. Mainen, T. J. Sejnowski, Synthesis of models for excitable membranes, synaptic transmission and neuromodulation using a common kinetic formalism. *J. Comput. Neurosci.* **1**, 195–230 (1994).
39. P. Poirazi, T. Brannon, B. W. Mel, Arithmetic of subthreshold synaptic summation in a model ca1 pyramidal cell. *Neuron* **37**, 977–987 (2003).
40. G. Stuart, N. Spruston, Determinants of voltage attenuation in neocortical pyramidal neuron dendrites. *J. Neurosci.* **18**, 3501–3510 (1998).
41. J. C. Magee, D. Johnston, Characterization of single voltage-gated na+ and ca2+ channels in apical dendrites of rat ca1 pyramidal neurons. *J. Physiol.* **487**, 67–90 (1995).
42. D. A. Hoffman, J. C. Magee, C. M. Colbert, D. Johnston, K+ channel regulation of signal propagation in dendrites of hippocampal pyramidal neurons. *Nature* **387**, 869–875 (1997).
43. M. Migliore, D. A. Hoffman, J. C. Magee, D. Johnston, Role of an a-type k+ conductance in the back-propagation of action potentials in the dendrites of hippocampal pyramidal neurons. *J. Comput. Neurosci.* **7**, 5–15 (1999).
44. J. C. Magee, Dendritic hyperpolarization-activated currents modify the integrative properties of hippocampal ca1 pyramidal neurons. *J. Neurosci.* **18**, 7613–7624 (1998).
45. J. C. Magee, E. P. Cook, Somatic epsp amplitude is independent of synapse location in hippocampal pyramidal neurons. *Nat. Neurosci.* **3**, 895–903 (2000).
46. B. K. Andrásfalvy, J. C. Magee, Distance-dependent increase in ampa receptor number in the dendrites of adult hippocampal ca1 pyramidal neurons. *J. Neurosci.* **21**, 9151–9159 (2001).
47. M. A. Smith, G. C. R. Ellis-Davies, J. C. Magee, Mechanism of the distance-dependent scaling of schaffer collateral synapses in rat ca1 pyramidal neurons. *J. Physiol.* **548**, 245–258 (2003).
48. D. A. Nicholson *et al.*, Distance-dependent differences in synapse number and ampa receptor expression in hippocampal ca1 pyramidal neurons. *Neuron* **50**, 431–442 (2006).
49. N. T. Carnevale, M. L. Hines, *The NEURON Book* (Cambridge University Press, 2006).

PNAS
www.pnas.org

Supplementary Information for

Dendritic computations captured by an effective point neuron model

Songting Li, Nan Liu, Xiaohui Zhang, David McLaughlin, Douglas Zhou, and David Cai

X. Z. xhzhang@bnu.edu.cn
D.M. david.mclaughlin@nyu.edu
D.Z. zdz@sjtu.edu.cn

This PDF file includes:

Supporting Information Text

Derivation of the synaptic integration current. In the main text, we have demonstrated that the point neuron model without the synaptic integration current (Eqs. 1 and 2 in the main text) does not suffice to characterize the somatic voltage dynamics of a spatial neuron with dendrites. In addition, using both electrophysiological experiments and realistic neuron simulations, we have obtained a novel synaptic integration current form being capable of characterizing the synaptic current arriving at the soma when the spatial neuron receives synaptic inputs on its dendrites. A bilinear conductance relation is further obtained in experiments and realistic neuron simulations. Here we theoretically explain the origin of the synaptic integration current by performing the static two-port analysis.[1,2,3] When a neuron receives static synaptic inputs, the electrical circuit representation of the neuron and the corresponding variables used in our analysis are shown in Fig. S0 below.

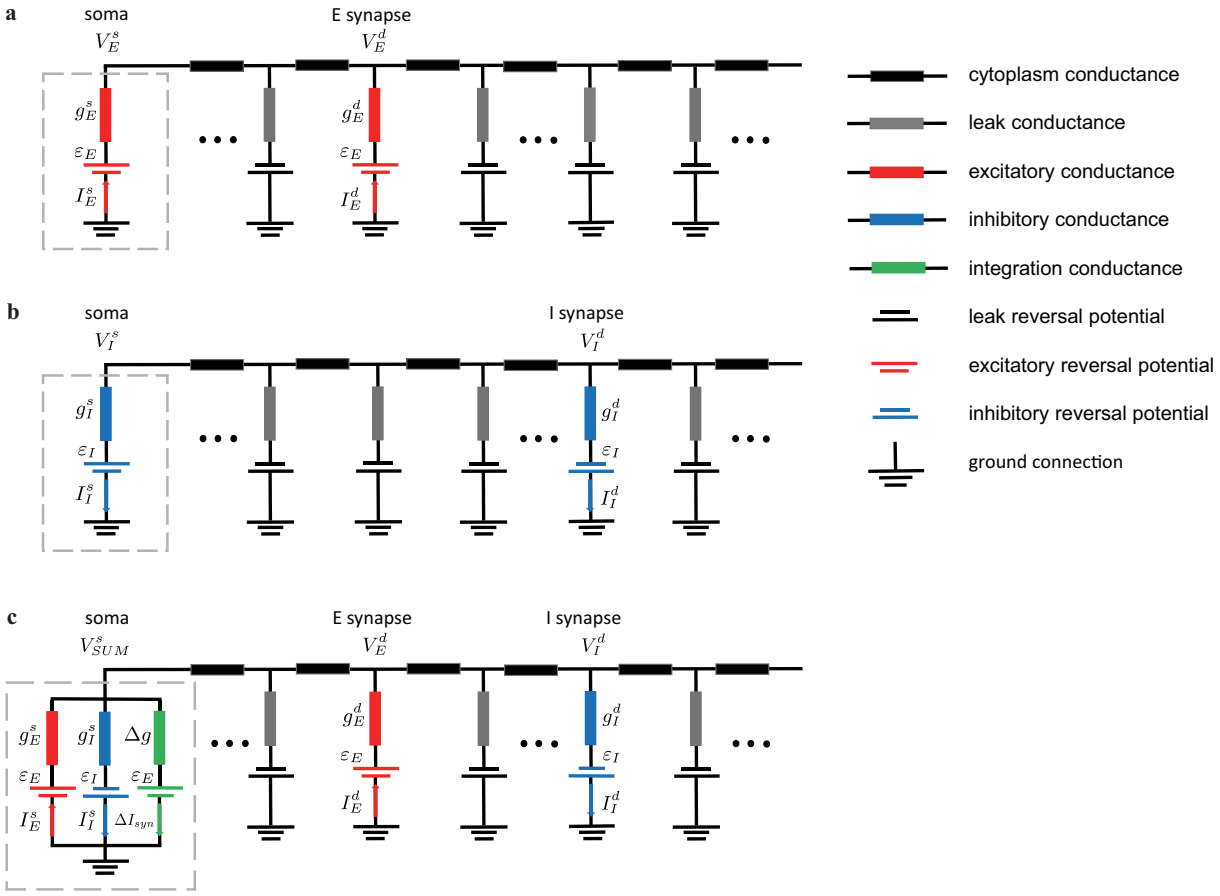

Fig. S0. Schematic diagram of the electrical circuit representation of a neuron when (**a**) an individual E input is received on the dendrite, (**b**) an individual I input is received on the dendrite, and (**c**) a pair of E and I inputs are received on the dendrite. The dashed grey boxes indicate the effective inputs received at the soma mapped from the local inputs on the dendrite (see text for details).

When a spatial neuron receives an excitatory (E) input on the dendrite, the local synaptic current on the dendrite I_E^d can be characterized by Ohm's law,

$$I_E^d = g_E^d(\varepsilon_E - V_E^d), \quad [1]$$

where g_E^d is the local E conductance on the dendrite, ε_E is the E reversal potential, and V_E^d is the local membrane potential on the dendrite. Here the superscript "d" emphasizes the quantities on the dendrite.

Based on Ohm's law, the local membrane potential V_E^d can be computed by

$$V_E^d = K_{EE} I_E^d, \quad [2]$$

where K_{EE} is the resistance at the E synapse. Therefore, combining Eqs. 1-2, the local membrane potential V_E^d is expressed as

$$V_E^d = \frac{g_E^d K_{EE} \varepsilon_E}{1 + g_E^d K_{EE}}. \quad [3]$$

Similarly, the excitatory postsynaptic potential (EPSP) V_E^s measured at the soma in response to the excitatory synaptic current I_E^d on the dendrite can be computed by

$$V_E^s = K_{ES} I_E^d, \tag{4}$$

where K_{ES} is the transfer resistance between the E synapse and the soma. The combination of Eqs. 1-4 yields the somatic membrane potential in response to the E input on the dendrite,

$$V_E^s = \frac{g_E^d K_{ES} \varepsilon_E}{1 + g_E^d K_{EE}}. \tag{5}$$

Now if we denote the synaptic current arriving at the soma as I_E^s that is induced by the synaptic current I_E^d (Eq. 1) from the dendrite, then based on Ohm's law, the synaptic current at the soma can be derived as

$$I_E^s = \frac{V_E^s}{K_{SS}}, \tag{6}$$

where K_{SS} is the resistance at the soma, the superscript "s" emphasizes the quantities at the soma.

If we further denote the E conductance measured at the soma as g_E^s, then g_E^s shall also obey Ohm's law

$$g_E^s = \frac{I_E^s}{\varepsilon_E - V_E^s}, \tag{7}$$

From Eqs. 5-7, we can obtain an expression for the E conductance g_E^s at the soma,

$$g_E^s = \frac{g_E^d K_{ES}}{K_{SS}\left[1 + g_E^d (K_{EE} - K_{ES})\right]} \tag{8}$$

Similarly, when a spatial neuron receives an inhibitory (I) input on its dendrites, the somatic membrane potential in response to the I input on the dendrite and the I conductance g_I^s measured at the soma can be derived as

$$V_I^s = \frac{g_I^d K_{IS} \varepsilon_I}{1 + g_I^d K_{II}}, \tag{9}$$

$$g_I^s = \frac{g_I^d K_{IS}}{K_{SS}\left[1 + g_I^d (K_{II} - K_{IS})\right]}, \tag{10}$$

where g_I^d is the local I conductance on the dendrite, K_{IS} is the transfer resistance between the I synaptic site and the soma, and K_{II} and K_{SS} are the resistances at the I synapse and the soma, respectively.

If we measure the E and I conductances g_E^s and g_I^s at the soma, from Eqs. 8 and 10, we are able to infer the local E and I conductances on the dendrite g_E^d and g_I^d as

$$g_E^d = \frac{g_E^s K_{SS}}{K_{ES} - g_E^s K_{SS}(K_{EE} - K_{ES})}, \tag{11}$$

$$g_I^d = \frac{g_I^s K_{SS}}{K_{IS} - g_I^s K_{SS}(K_{II} - K_{IS})}. \tag{12}$$

Now given a pair of E and I synaptic inputs on the dendrites of the spatial neuron with the same input locations and strengths as given separately, by Ohm's law, we have the local E and I synaptic currents on the dendrite

$$I_E^d = g_E^d(\varepsilon_E - V_E^d), \tag{13}$$

$$I_I^d = g_I^d(\varepsilon_I - V_I^d). \tag{14}$$

In Eqs. 13-14, the local membrane potentials measured at the E synapse V_E^d and at the I synapse V_I^d can be obtained as follows,

$$V_E^d = K_{EE} I_E^d + K_{IE} I_I^d, \tag{15}$$

$$V_I^d = K_{EI} I_E^d + K_{II} I_I^d. \tag{16}$$

By solving Eqs. 13-16, we can obtain the local synaptic currents on the dendrite as

$$I_E^d = \frac{g_E^d \varepsilon_E + g_E^d g_I^d (K_{II}\varepsilon_E - K_{EI}\varepsilon_I)}{1 + g_E^d K_{EE} + g_I^d K_{II} + g_E^d g_I^d (K_{EE}K_{II} - K_{EI}^2)}, \tag{17}$$

$$I_I^d = \frac{g_I^d \varepsilon_I + g_E^d g_I^d (K_{EE}\varepsilon_I - K_{EI}\varepsilon_E)}{1 + g_E^d K_{EE} + g_I^d K_{II} + g_E^d g_I^d (K_{EE}K_{II} - K_{EI}^2)}. \tag{18}$$

By Ohm's law together with the local synaptic current expressions (17-18), we can further solve the membrane potential at the soma as

$$\begin{aligned} V^s_{SUM} &= K_{ES} I^d_E + K_{IS} I^d_I \\ &= \frac{g^d_E K_{ES}\varepsilon_E + g^d_I K_{IS}\varepsilon_I + g^d_E g^d_I \left[\varepsilon_E (K_{II}K_{ES} - K_{IS}K_{EI}) + \varepsilon_I (K_{EE}K_{IS} - K_{ES}K_{EI})\right]}{1 + g^d_E K_{EE} + g^d_I K_{II} + g^d_E g^d_I (K_{EE}K_{II} - K^2_{EI})}, \end{aligned} \tag{19}$$

V^s_{SUM} has been referred to as the summed somatic potential (SSP) in the main text.

On the one hand, by using the SSP expression (19), we can obtain the summed somatic current (SSC) denoted as $I^s_{SUM} = V^s_{SUM}/K_{SS}$; on the other hand, by using Eqs. 8, 10 and 19, we can reconstruct the EPSC and IPSC at the soma as $I^s_E = g^s_E(\varepsilon_E - V^s_{SUM})$ and $I^s_I = g^s_I(\varepsilon_I - V^s_{SUM})$, respectively.

Through calculations, we can show that the SSC is not equal to the linear summation of the EPSC and the IPSC. The difference between them, i.e., the synaptic integration current, can be expressed as

$$\begin{aligned} \Delta I_{syn} &= I^s_{SUM} - I^s_E - I^s_I \\ &= \frac{g^d_E g^d_I (A + g^d_E B + g^d_I C + g^d_E g^d_I D)}{K_{SS}\left[1 + g^d_E (K_{EE} - K_{ES})\right]\left[1 + g^d_I (K_{II} - K_{IS})\right]\left[1 + g^d_E K_{EE} + g^d_I K_{II} + g^d_E g^d_I (K_{EE}K_{II} - K^2_{EI})\right]} \end{aligned}$$

where

$$\begin{aligned} A &= \varepsilon_E K_{IS}(K_{ES} - K_{EI}) + \varepsilon_I K_{ES}(K_{IS} - K_{EI}), \\ B &= \varepsilon_E \left[K_{ES}K_{IS}(K_{EE} - K_{ES}) + K_{EI}(K_{EI}K_{ES} - K_{EE}K_{IS})\right] + \varepsilon_I K_{EE}K_{ES}(K_{IS} - K_{EI}), \\ C &= \varepsilon_I \left[K_{ES}K_{IS}(K_{II} - K_{IS}) + K_{EI}(K_{EI}K_{IS} - K_{II}K_{ES})\right] + \varepsilon_E K_{II}K_{IS}(K_{ES} - K_{EI}), \\ D &= \varepsilon_E \left[K^2_{EI}K_{ES}(K_{II} - K_{IS}) + K_{EE}K_{II}K_{IS}(K_{ES} - K_{EI}) + K_{ES}K_{IS}(K_{EI}K_{IS} - K_{ES}K_{II})\right] \\ &+ \varepsilon_I \left[K^2_{EI}K_{IS}(K_{EE} - K_{ES}) + K_{EE}K_{II}K_{ES}(K_{IS} - K_{EI}) + K_{ES}K_{IS}(K_{EI}K_{ES} - K_{IS}K_{EE})\right]. \end{aligned}$$

We note that, the synaptic integration current ΔI_{syn} vanishes when the E and I inputs are given at the soma, where $A = B = C = D = 0$. To the leading order of the input conductances, the synaptic integration current ΔI_{syn} is proportional to the multiplication of the E and I conductances on the dendrite,

$$\Delta I_{syn} = \frac{A}{K_{SS}} g^d_E g^d_I + o(g^d_E g^d_I). \tag{20}$$

If we further cast the synaptic integration current ΔI_{syn} in the form of Ohm's law, i.e., $\Delta I_{syn} = \Delta g(\varepsilon_E - V^s_{SUM})$, then we have

$$\begin{aligned} \Delta g &= \frac{\Delta I_{syn}}{\varepsilon_E - V^s_{SUM}} \\ &= \frac{A}{\varepsilon_E K_{SS}} g^d_E g^d_I + o(g^d_E g^d_I) \\ &= \frac{A K_{SS}}{\varepsilon_E K_{ES} K_{IS}} g^s_E g^s_I + o(g^s_E g^s_I) \end{aligned} \tag{21}$$

The second equality in Eq. 21 holds by viewing the ratio V^s_{SUM}/ε_E as a small variable and performing Taylor expansion to the first order. the The last equality in Eq. 21 holds because of Eqs. 11-12. We thus have explained the bilinear conductance relation observed in both the electrophysiological experiments and the realistic neuron simulations, i.e.,

$$\Delta g = \alpha_{EI} g^s_E g^s_I, \tag{22}$$

where the integration coefficient α_{EI} can be explicitly expressed as

$$\alpha_{EI} \approx K_{SS}\left(1 - \frac{K_{EI}}{K_{ES}}\right) + K_{SS}\frac{\varepsilon_I}{\varepsilon_E}\left(1 - \frac{K_{EI}}{K_{IS}}\right). \tag{23}$$

From the above expression (23), the integration coefficient α_{EI} vanishes when the E and I inputs are given at the soma. On account of the fact that ε_E is almost one order of magnitude larger than ε_I, the expression for the coefficient could be further simplified as

$$\alpha_{EI} \approx K_{SS}\left(1 - \frac{K_{EI}}{K_{ES}}\right).$$

Note that when the synaptic integration current is cast in the form of Ohm's law, the reversal potential is set to be the excitatory reversal potential ε_E. In fact, there is a degree of freedom for choosing the value of the reversal potential ε within the regime in which the ratio V^s_{SUM}/ε is much smaller than unity in order to make the Taylor expansion in Eq. 21 accurate. Correspondingly, the value of the integration coefficient α_{EI} depends on the choice of the reversal potential. However, we stress that the bilinear relation of the conductances (22) remains valid when choosing a different reversal potential value.

Spatial dependence of the integration coefficients. Note that the transfer function K_{EI} decreases as the distance between the E and I input locations increases, and K_{ES} decreases as the distance between the E input location and the soma increases. Therefore, in general, α_{EI} is large negative for E and I inputs spatially close to each other at distal dendrite and it is less negative for E and I inputs spatially separated away from each other at proximal dendrite. In particular, when the I input location is fixed on the dendritic trunk and the E input location is between the soma and the I input location, as the distance between the E input location and the soma increases, K_{EI} in the numerator increases while K_{ES} in the denominator decreases, hence the decrease of α_{EI}; when the E input location is further away from the soma than the I input location, as the distance between the E input location and the soma increases, both K_{EI} in the numerator and K_{ES} in the denominator decreases, hence α_{EI} remains almost constant. This explains the spatially asymmetric dependence of α_{EI} as observed in the realistic neuron simulation in the main text. In addition, in general, a neuron receives E inputs at distal dendrites while receives I inputs at proximal dendrites. In such a case, $K_{EI} > K_{ES}$. Therefore, α_{EI} is mostly negative.

Similarly, for a pair of inputs of the same type, we can also derive the bilinear form of the integration conductance as

$$\Delta g = \alpha_{Q_1Q_2} g^s_{Q_1} g^s_{Q_2},$$

where $Q = E, I$ represents the input type, and the integration coefficient $\alpha_{Q_1Q_2}$ can be expressed as

$$\begin{aligned} \alpha_{Q_1Q_2} &\approx \frac{K_{SS}\left[K_{Q_2S}(K_{Q_1S}-K_{Q_1Q_2})+K_{Q_1S}(K_{Q_2S}-K_{Q_1Q_2})\right]}{K_{Q_1S}K_{Q_2S}} \\ &= K_{SS}\left(2-\frac{K_{Q_1Q_2}}{K_{Q_1S}}-\frac{K_{Q_1Q_2}}{K_{Q_2S}}\right), \end{aligned} \quad [24]$$

from which we can see that $\alpha_{Q_1Q_2}$ is smaller for both inputs spatially close to each other at distal dendrite than those spatially separated away from each other at proximal dendrite. In particular, when the input location of Q_1 is fixed at the dendritic trunk while the input location of Q_2 is between the soma and that of Q_1, as the distance between the location of Q_2 and the soma increases, $K_{Q_1Q_2}$ increases but K_{Q_2S} decreases, hence the decrease of $\alpha_{Q_1Q_2}$; when the input location of Q_2 is further away from the soma than that of Q_1, as the distance between the location of Q_2 and the soma increases, both $K_{Q_1Q_2}$ and K_{Q_2S} decreases, which results in the decrease of the term $\frac{K_{Q_1Q_2}}{K_{Q_1S}}$ and almost no change of the term $\frac{K_{Q_1Q_2}}{K_{Q_2S}}$, hence the increase of $\alpha_{Q_1Q_2}$. This explains the spatially symmetric dependence of α_{EE} and α_{II} as observed in the realistic neuron simulation in the main text.

Bilinear dendritic integration rule. Previous experiments[2,4] showed that when a neuron receives a pair of E and I inputs, the SSP denoted by V_S can be well characterized by the following bilinear integration rule,

$$V^s_{SUM} = V^s_E + V^s_I + k_{EI} V^s_E V^s_I$$

where V^s_E and V^s_I denote the somatic EPSP and IPSP induced by the E and I inputs given alone respectively, and k_{EI} is the shunting coefficient independent of input strengths but dependent of input time and locations.

The above rule can be captured in the point neuron model by incorporating the synaptic integration current, and there is a one-to-one mapping between the shunting coefficient and the integration coefficient that can be derived in the following. Using the approximations of EPSP, IPSP, and SSP (Eqs. 5, 9 and 19), we can obtain the expression of the shunting coefficient k_{EI}

$$k_{EI} = \frac{V^s_{SUM} - V^s_E - V^s_I}{V^s_E V^s_I} \approx -\frac{K_{IE}}{K_{IS}\varepsilon_E} - \frac{K_{EI}}{K_{ES}\varepsilon_I}. \quad [25]$$

This explains the experimental observation that the SSP follows a bilinear integration rule with the shunting coefficient being independent of synaptic input strengths but dependent of the synaptic input locations. From Eqs. 23 and 25, we can directly obtain the one-to-one linear mapping between the integration coefficient and the shunting coefficient,

$$\alpha_{EI} \approx K_{SS}\varepsilon_I\left(\frac{\varepsilon_E + \varepsilon_I}{\varepsilon_E\varepsilon_I} + k_{EI}\right)$$

Therefore, the shunting coefficient k_{EI} exhibits the same spatially asymmetric feature as the integration coefficient α_{EI} as explained from our two-port analysis in the above.

Direction selectivity. Here we illustrate the capability of direction selectivity[5,6] of our point neuron model as discussed in the main text. For the sake of illustration, we consider the idealized case that the decay time constant of the membrane potential is extremely fast. In this case, on the one hand, if multiple E synaptic inputs are received by the neuron at different times, the last pair of E inputs will dominantly contribute to the somatic membrane potential at the time right after the last E input is received, because the membrane potential change induced by all the previous inputs decays rapidly. On the other hand, as an E input moves away from the soma towards the distal dendrite, K_{ES} becomes smaller. According to Eq. 24, α_{EE} in the point neuron model is larger negative for a pair of E inputs located at distal dendrite than that at proximal dendrite. Therefore,

the sequential activation of synaptic inputs in the direction from distal to proximal dendrites (whose effect will be dominated by the last pair of inputs at proximal dendrite with a small negative coefficient) gives rise to larger somatic response than the sequential activation of synaptic inputs in the reversed direction (whose effect will be dominated by the last pair of inputs at distal dendrite with a large negative coefficient). This enables the point neuron to perform the computation of direction selectivity.

Coincidence detection. Here we illustrate the capability of coincidence detection[7] of our point neuron model as discussed in the main text. For the sake of illustration, we consider the idealized case that a spatial neuron has two identical dendritic branches connecting to its soma. On the one hand, we have $K_{E_1S} = K_{E_2S}$ and a large $K_{E_1E_2}$ when two E inputs are received at the same location on a branch; on the other hand, we have $K_{E_1S} = K_{E_2S}$ and a small $K_{E_1E_2}$ when two E inputs are received on two different branches with equal distance to the soma. Therefore, from Eq. 24, α_{EE} in our point neuron model is large negative for two E inputs received on the same branch from one ear and it is nearly positive for two E inputs received on two separate branches from both ears. Therefore, the neuron's membrane potential may stay below the firing threshold when receiving two E inputs on the same branch, while it may cross the firing threshold when receiving two E inputs on two separate branches. This enables the point neuron to perform coincidence detection of inputs from both ears.

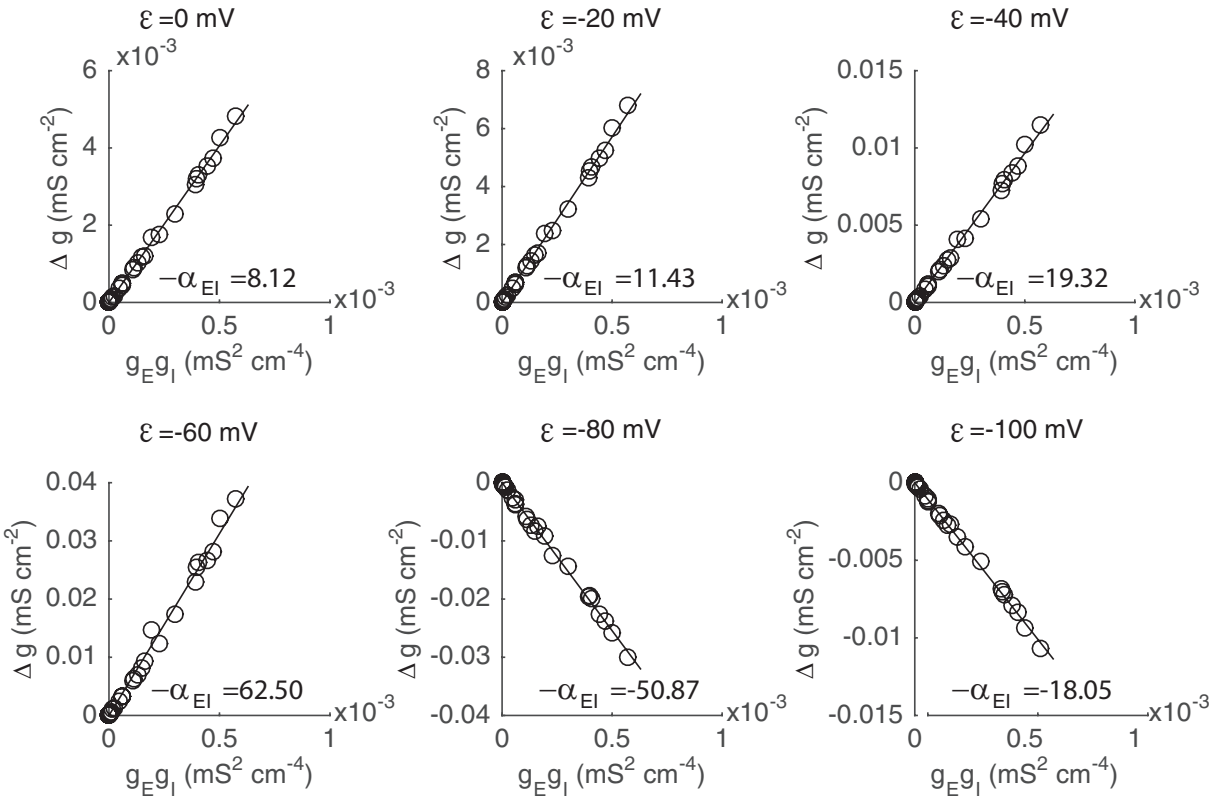

Fig. S1. The validity of the bilinear relation between Δg and the multiplication of g_E and g_I for different choice of reversal potential values ε in the synaptic integration current $\Delta I_{syn} = \Delta g(\varepsilon - V)$. The same data set is used here as that in Fig. 2c in the main text. The value of the reversal potential ranges from 0 mV to -100 mV. The corresponding integration coefficient value α_{EI} is specified within each figure panel with the unit of $\mathrm{k}\Omega \cdot \mathrm{cm}^2$.

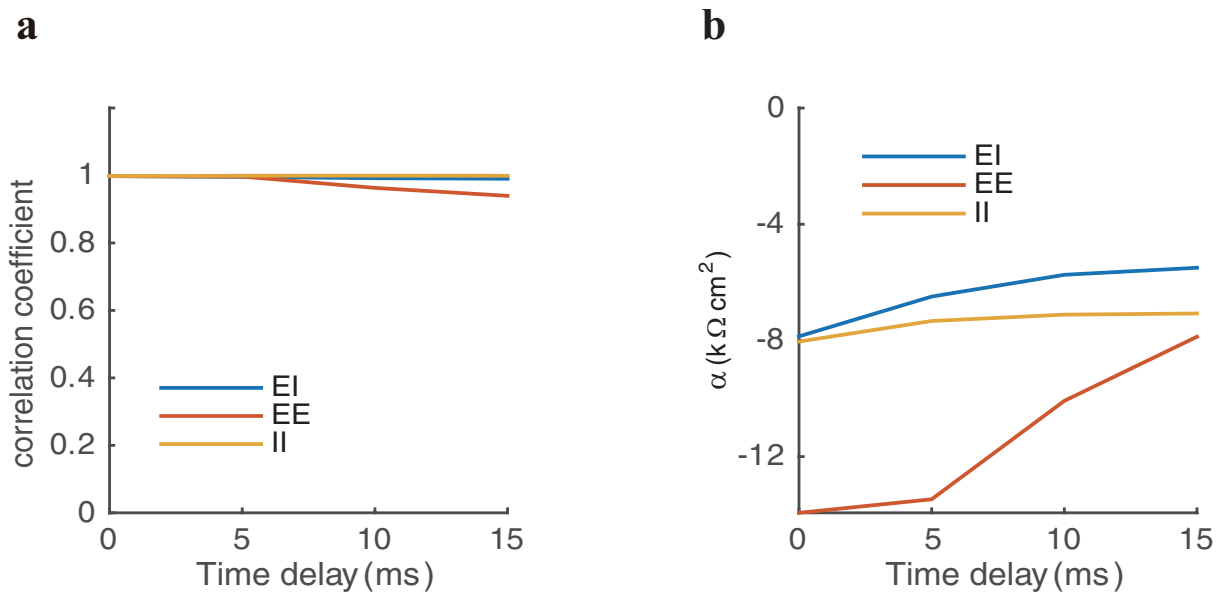

Fig. S2. The dependence of integration coefficients on the arrival time difference between a pair of E and I inputs, two E inputs, and two I inputs. **a**, the correlation coefficient between the integration conductance Δg and the product of the two individual conductances as a function of the time difference between the two inputs. **b**, the integration coefficient as a function of the time difference between the two inputs. All the data are measured at the peak time of an E conductance (for the EI and EE cases) or the peak time of an I conductance (for the II case).

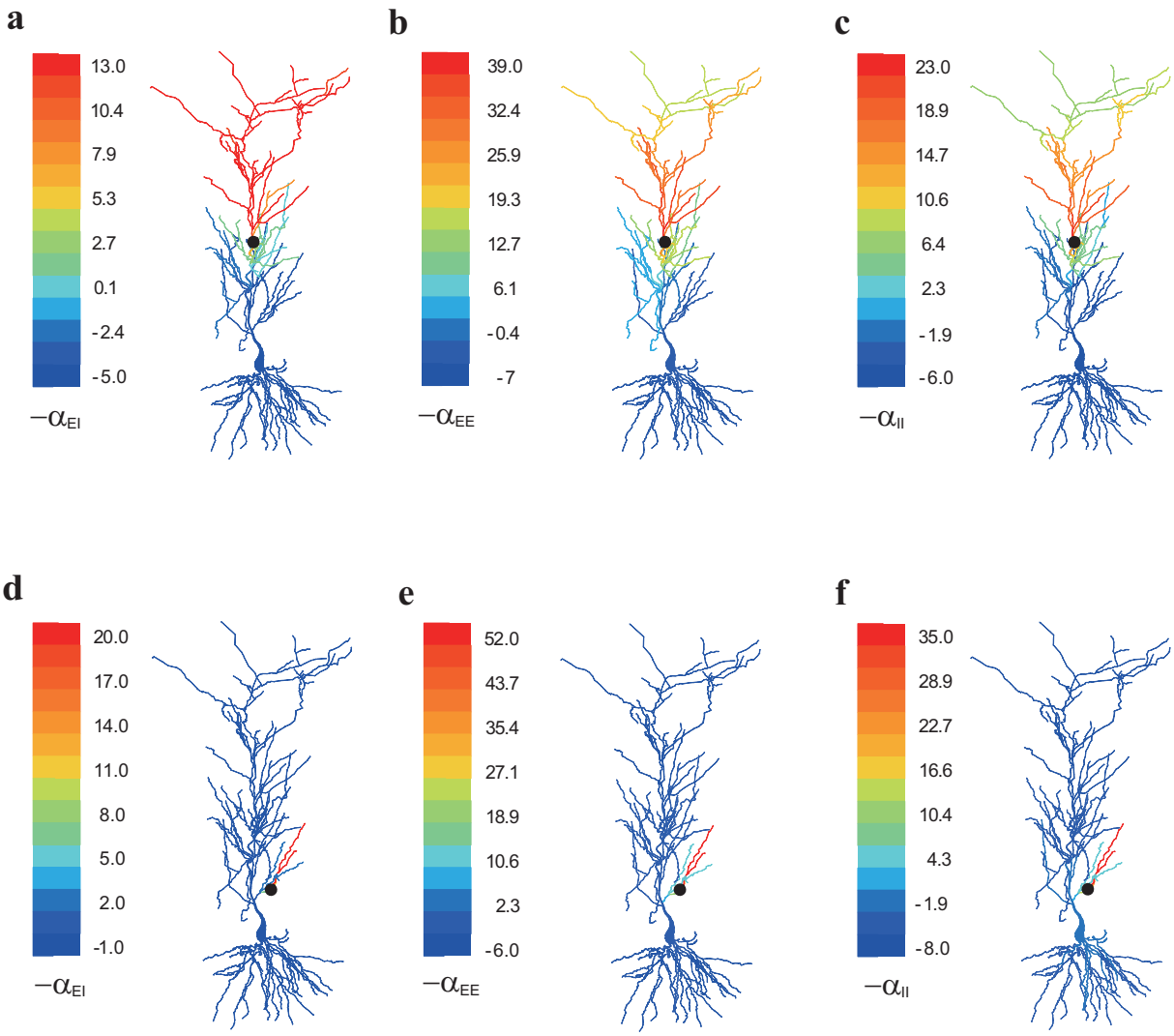

Fig. S3. The spatial profile of the integration coefficients in the whole dendrites. **a**, the spatial profile of $-\alpha_{EI}$ with the I input fixed at the dendritic trunk marked by the black dot and the E input scattered on the dendrites. **b-c**, the spatial profile of $-\alpha_{EE}$ and $-\alpha_{II}$ with one E (I) input fixed at the dendritic trunk marked by the black dot and the other E(I) input scattered on the dendrites. **d-f**, the same as **a-c** except that one input is fixed at a dendritic branch rather than at the dendritic trunk.

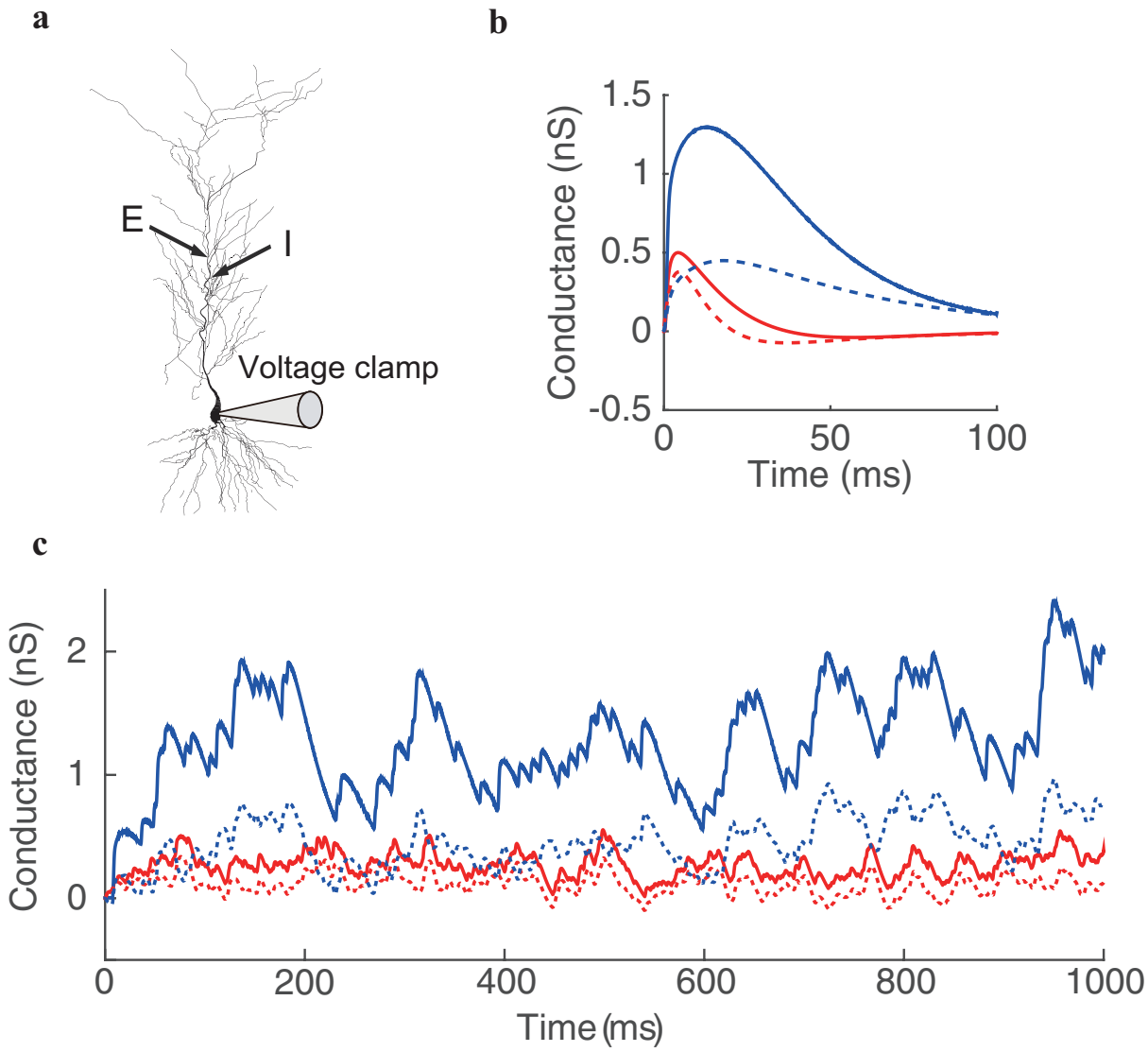

Fig. S4. The issue of conductance measurement based on the assumption of linear summation of E and I synaptic currents. **a**, the recording configuration when the realistic neuron model receives a pair of E and I inputs. A voltage clamp is made at the soma. Somatic voltage is clamped from -60 mV to -100 mV with a decrement of -10 mV when both the E and I inputs are given simultaneously at the dendritic trunk 350 μm and 280 μm away from the soma. The arrows indicate the locations of the E and I inputs. **b**, the recovered E conductance (dash red) and I conductance (dash blue) based on the form of linear summation of E and I synaptic currents when a pair of transient E and I inputs are given simultaneously at the locations indicated in **a**. The reference E conductance (solid red) and I conductance (solid blue) are calculated from the point neuron model when the E or I input is given separately in the realistic neuron model. **c**, the same as **b** except that the neuron receives two spike trains as the inputs. The input times at each location are uniformly distributed from 0 ms to 1000 ms. The rate of the E input is 400 Hz and that of the I input is 100 Hz at each input location.

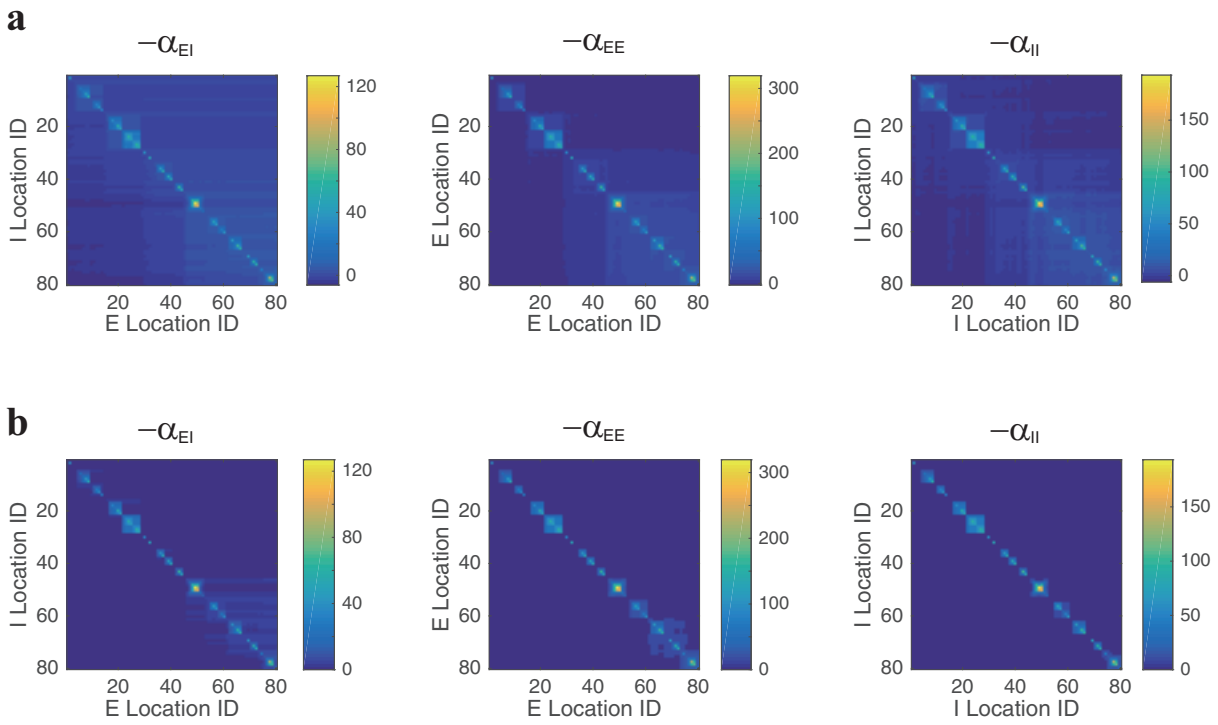

Fig. S5. The sparsity of the integration coefficient matrices. **a**, the measured integration coefficient matrices for $-\alpha_{EI}$, $-\alpha_{EE}$, and $-\alpha_{II}$. An element in each matrix corresponds to an integration coefficient measured in the realistic neuron model given a pair of inputs at its dendritic arbor in *stratum radiatum*. The labels of the x-axis and the y-axis of each matrix are the ID number of the dendritic compartment in the model. In general, two compartments are physically close to each other if their ID numbers are close, and one compartment is further away from the soma than another compartment if its ID number is larger than that of another compartment. **b**, the same as **a** except that the minus of the coefficients below a threshold in each matrix are set to be zero. The thresholds are determined as that the integration coefficient is significantly nonzero such that the bilinear integration of synaptic currents only leads to a change of SSP greater than 5%, given an EPSP of 4 mV and an IPSP of -1 mV. The value of the threshold is 3.13 k$\Omega \cdot \mathrm{cm}^2$ for the E-I case, 16.72 k$\Omega \cdot \mathrm{cm}^2$ for the E-E case, and 9.89 k$\Omega \cdot \mathrm{cm}^2$ for the I-I case. The percentage of nonzero coefficients in each matrix is 15.33% for the E-I case, 7.39% for the E-E case, and 4.67% for the I-I case, which is sparse.

References

1. Koch C (2004) *Biophysics of computation: information processing in single neurons.* (Oxford university press).
2. Hao J, Wang Xd, Dan Y, Poo Mm, Zhang Xh (2009) An arithmetic rule for spatial summation of excitatory and inhibitory inputs in pyramidal neurons. *Proceedings of the National Academy of Sciences* 106(51):21906–21911.
3. Zhou D, Li S, Zhang Xh, Cai D (2013) Phenomenological incorporation of nonlinear dendritic integration using integrate-and-fire neuronal frameworks. *PloS one* 8(1):e53508.
4. Li S, Liu N, Zhang Xh, Zhou D, Cai D (2014) Bilinearity in spatiotemporal integration of synaptic inputs. *PLoS computational biology* 10(12):e1004014.
5. Barlow HB, Hill RM (1963) Selective sensitivity to direction of movement in ganglion cells of the rabbit retina. *Science* 139(3553):412–412.
6. Vaney DI, Taylor WR (2002) Direction selectivity in the retina. *Current opinion in neurobiology* 12(4):405–410.
7. Agmon-Snir H, Carr CE, Rinzel J (1998) The role of dendrites in auditory coincidence detection. *Nature* 393(6682):268.